

Activity Indices Based on Sun-as-a-Star Spectra Obtained with the SOLIS Integrated Sunlight Spectrometer

Masterarbeit

in der Wissenschaftsdisziplin Astronomie und Astrophysik

eingereicht an der

Mathematisch-Naturwissenschaftlichen Fakultät
der Universität Potsdam

Erstgutachter und Betreuer: apl. Prof. Dr. Carsten Denker

Zweitgutachter: apl. Prof. Dr. Gottfried Mann

Linh Le Phuong

May 14, 2016



Leibniz-Institut für Astrophysik Potsdam
An der Sternwarte 16
14482 Potsdam



Universität Potsdam, Campus Golm
Institut für Physik und Astronomie (Haus 28)
Karl-Liebnecht-Strasse 24/25
14476 Potsdam-Golm

Table of Contents

Abstract	1
Zusammenfassung	3
1 Stars and the Sun	5
1.1 The Way of a Star – the Hertzsprung Russel Diagram	5
1.2 Continuous Radiation from Stars	7
1.3 Limb Darkening	8
1.4 Radiative Transfer Theory and Spectral Lines	9
1.4.1 Radiative Transfer Theory	10
1.4.2 Spectral Lines and Line Broadening	11
2 The Sun	15
2.1 Sun-as-a-Star Observations	15
2.2 Solar Structure	15
2.2.1 Solar Interior	16
2.2.2 Solar Atmosphere	16
2.3 Solar Cycle	19
2.3.1 Sunspot Number	19
2.3.2 Solar Irradiance	19
3 Chromospheric Features	21
4 Integrated Sunlight Spectrometer	23
5 Sun-as-a-Star Spectra	27
6 Activity Indices	35
6.1 Sunspot Number	35
6.2 F10.7 cm Radio Flux	37
6.3 Mg II Index	38
6.4 Total Solar Irradiance	39
6.5 Linear Regressions and Correlation Coefficients of Scatterplots	42
7 Activity Index from Hα	47
7.1 Cloud Model	47
7.2 Hα Centre-to-Limb Variation	48

7.3 Contrast Profiles	50
8 Conclusion	58
Bibliography	61
Acknowledgments	65
Appendix A – List of Acronyms	67

Abstract

Context The Sun is only an average star, but the Earth's main energy source and therefore influences our lives in many respects. Consequently, understanding its activity variations is important to us. Unlike other stars, however, we can observe the Sun in greater detail and have disk-resolved spectra, which allows investigations of particular solar regions or features. Thus, we can infer other activity indices than just the Total Solar Irradiance (TSI). For other stars, however, we only have disk-integrated spectra to make conclusions about their properties. If we can use the solar disk-integrated spectrum, find indices for the solar activity (by investigating the changes in the spectrum) and connect this to solar disc-resolved observations, we hope to be able to relate this to other stars and make suggestions about their disk-resolved properties and activity. Sun-as-a-star activity indices derived from solar integrated spectra in the Ca II K line do already exist.

Aims The purpose of this work is to find chromospheric activity indices with H α Sun-as-a-star spectra, to help draw conclusions about the activity of other stars, which have only the integrated spectra available. In addition, we want to examine the physical constitution that results in these spectra by applying an inversion technique known as the Cloud Model (CM).

Methods In this thesis we used mainly H α and Ca II K data from the Integrated Sunlight Spectrometer (ISS) as part of the Synoptic Optical Long-term Observations of the Sun (SOLIS). First, we reconstructed the plots that present chromospheric activity indices of the Ca II K line, found in Bertello *et al.* (2011). We do this, to make sure that we are handling the data correctly, as we use the data of the same instrument, to find our index. Unlike in Bertello *et al.* (2011), our plots show the time series of the parameters for a longer time period, from 2007–2015. We, furthermore, investigated other activity indices, which each represent a different atmospheric layer of the Sun. These investigation regard the sunspot number, the F10.7 cm Radio Flux, the Mg II index, as well as the Total Solar Irradiance (TSI), their variation with time and correlation with each other. Eventually, we want to be able to compare our index with the already existing ones. To find our index, we fitted the H α Sun-as-a-Star spectra with a triple Voigt function and calculated the contrast profile. Plotting the total contrast as a function of time gives us the light curve of our index and reveals the change of the contrast with time. We then applied Beckers Cloud Model (CM) (Beckers, 1964) to obtain parameters for the structure where the line evolves and derive physical explanations for it. Finally, we created scatter plots of our index with the sunspot number to see how the two indices and the corresponding atmospheric layers correlate.

Results Our reconstruction of the plots found in Bertello *et al.* (2011), shows that we handled the data correctly. With the data of the same instrument (ISS) we calculated the total contrast, where the total contrast around the line core is our index. Creating the scatter plot of the H α index with the sunspot number shows a good correlation between them, with a correlation coefficient of $r = 0.686$. This means that what we found is indeed an index for the chromospheric activity, which also correlates with the photospheric activity and hence reveals the connection between chromospheric and photospheric activity. However, applying Beckers' CM to fit the contrast profile and obtain physical parameters did not lead to fully reasonable results and needs

further investigation.

Conclusions Besides Ca II K indices, Sun-as-a-star chromospheric activity indices can be found in the H α line, derived from the contrast profiles of the daily integrated spectrum and the averaged quiet Sun, each in H α . This can be applied to other stars and their spectrum as well to make suggestions about their properties. To make conclusion about the physical explanation of this index, an improved fitting of the contrast profiles and the physical parameters, derived from the CM, for all of our contrast profiles are needed.

Zusammenfassung

Kontext Die Sonne ist eigentlich nur ein durchschnittlicher Stern, jedoch ist sie auch die Hauptenergiequelle der Erde und beeinflusst unser Leben auf vielerlei Weise. Ein gutes Verständnis über ihre Aktivität ist für uns von daher sehr wichtig. Im Gegensatz zu anderen Sternen lässt sich die Sonne detaillierter beobachten, was die Untersuchung von bestimmten Regionen auf der Sonne und ihren Merkmalen ermöglicht. Somit können wir neben der Total Solar Irradiance (TSI) noch andere Indizes ermitteln. Für andere Sterne jedoch haben wir nur die integrierten Spektren, um Eigenschaften zu untersuchen. Wenn wir nun die integrierten Spektren nutzen und Aktivitätsindizes finden, indem wir die Änderung der Spektren untersuchen, können wir diese wissenschaftlichen Errungenschaften auf Sternspektren anwenden und Vermutungen im Hinblick auf ihre feinen Merkmale und Strukturen aufstellen. Aktivitätsindizes für die Sonne als Stern existieren bereits, abgeleitet von der Ca II K-Linie.

Ziele Diese Arbeit zielt darauf ab, Indizes für die Aktivität der Chromosphäre der Sonne mit Scheiben-integrierten H α -Spektren zu finden. Dies soll dazu dienen, Schlüsse über die Aktivität von anderen Sternen zu ziehen, für welche wir nur die integrierten Spektren beobachten können. Zusätzlich möchten wir die physikalischen Gegebenheiten untersuchen, die zum Entstehen dieser Spektren beitragen, indem wir die Inversionstechnik anwenden, welche das Cloud Model (CM) genannt wird.

Methoden In dieser Arbeit nutzten wir hauptsächlich H α und Ca II K-Daten vom Integrated Sunlight Spectrometer (ISS), welches Teil des Synoptic Optical Long-Term Investigations of the Sun (SOLIS) ist. Zuerst rekonstruierten wir die Abbildungen aus Bertello *et al.* (2011), welche die chromosphärischen Aktivitätsindizes der Ca II K-Linie repräsentieren. Dies diente der Überprüfung dessen, ob wir mit den Daten korrekt umgehen. Im Gegensatz zu Bertello *et al.* (2011) zeigen unsere Abbildungen die Zeitreihen der Indizes für einen verlängerten Zeitraum von 2007 – 2015. Außerdem untersuchten wir weitere Aktivitätsindizes, welche jeweils eine andere Atmosphärenschicht der Sonne repräsentieren. Diese Untersuchung galt der Sonnenfleckenanzahl, dem F10.7 cm Radio Fluss Index, dem Mg II Index, der gesamten Sonneneinstrahlung (Total Solar Irradiance - TSI) als auch ihrer Veränderung mit der Zeit und ihrer Korrelation miteinander. Letztendlich wollen wir unseren Index mit diesen Indizes vergleichen. Um unseren Index zu finden, passten wir die H α -Spektren mit einer dreifachen Voigt Funktion an und berechneten das Kontrastprofil. Der totale Kontrast als Funktion der Zeit gibt uns die Zeitreihe für unseren Index. Wir verwendeten Beckers' Cloud Model (Beckers, 1964), um Parameter für die gegebene Struktur (wo unsere Spektrallinien entstehen) und dadurch auch eine physikalische Erklärung für unseren Index zu erhalten. Zum Schluss kreierten wir ein Streudiagramm unseres Indexes mit der Sonnenfleckenanzahl, um zu sehen, wie gut diese beiden und damit ihre zugehörigen Schichten korrelieren.

Ergebnisse Die Rekonstruktionen der Abbildungen aus Bertello *et al.* (2011) zeigen, dass wir mit den Daten richtig umgegangen sind. Mit den Daten für H α berechneten wir den totalen Kontrast, welcher unserem Index entspricht. Das Streudiagramm unseres Indexes mit der Sonnenfleckenanzahl weist eine gute Korrelation zwischen diesen beiden auf, mit einem Korrelations-

skoeffizienten von $r = 0.686$. Dies bedeutet, dass unser Index tatsächlich ein Index für die Aktivität in der Chromosphäre ist, aber auch mit der photosphärischen Aktivität zusammenhängt. Die Anwendung des CM, um das Kontrastprofil anzupassen, führte nicht zu soliden Ergebnissen und bedarf weiterer Untersuchungen.

Schlussfolgerung Chromosphärische Aktivitätsindizes für die Sonne-als-Stern können im $H\alpha$ gefunden werden, abgeleitet von den Kontrastprofilen des täglichen Spektrums und des Referenzprofils der ruhigen Sonne. Dieses Wissen können wir auf das Spektrum anderer Sterne, zur Untersuchung ihrer Eigenschaften anwenden. Um Schlüsse über die physikalische Erklärung ziehen zu können, brauchen wir eine verbesserte Anpassung der Spektren und die Parameter, abgeleitet von dem CM für alle unsere Kontrastprofile.

Chapter 1

Stars and the Sun

The Sun is only one out of 10^{11} stars in our Galaxy, the Milky Way (Hanslmeier, 2002, p. 4). Yet, the Sun is very special for us, as it is the main energy source for Earth, and therefore a precondition for life on Earth. Just as other stars, the Sun was formed in a cloud of molecular gas. Molecular clouds are, compared to the interstellar medium, dense regions with about 10^{12} molecules per cubic metre (Ward-Thompson and Whitworth, 2011, p. 4–5). The gravitational attraction between the particles in the cloud keeps the cloud together. It is in hydrostatic equilibrium, if the kinetic energy of the gas pressure and the potential energy of the gravitational force are in balance. Furthermore, a cloud is gravitationally bound, if the gravitational forces are greater than the gas pressure that drives the particles apart. Hence, if the gas pressure is greater, the cloud will expand, but once it is gravitationally bound, it is gravitationally unstable and thus the cloud will begin to collapse and then form stars like our Sun (Kutner, 2003, p. 263).

How the stars exactly emerge from these clouds is not fully understood yet. But eventually all stars will end up on the main sequence of the Hertzsprung Russel Diagram (HRD), where the star's position on the main sequence is determined by its mass (Ward-Thompson and Whitworth, 2011, p. 177). The following chapter is intended to give an overview of the main characteristics of the Sun, partly in relation to other stars, by placing it in the HRD and explaining the radiative transfer in stars.

1.1 The Way of a Star – the Hertzsprung Russel Diagram

To briefly sum up the evolution of a star, the Sun and other stars are born in clouds of molecular gas, live a life that depends on their mass, and die according to it as well. In any case, a star will always exist, even if just for a short period, on the main sequence of the HRD, which is shown in Fig. 1.1.

In the HRD stars are divided in spectral classes or spectral types. At first, the spectra of the stars were classified according to the strongest hydrogen absorption lines, thus A stars had the strongest hydrogen lines, B stars had the next strongest, and so on. Today, spectral types are arranged according to the effective temperature (Kutner, 2003, p. 26), which gives the following sequence: O B A F G K M, starting with the hottest stars (early types) and ending with the

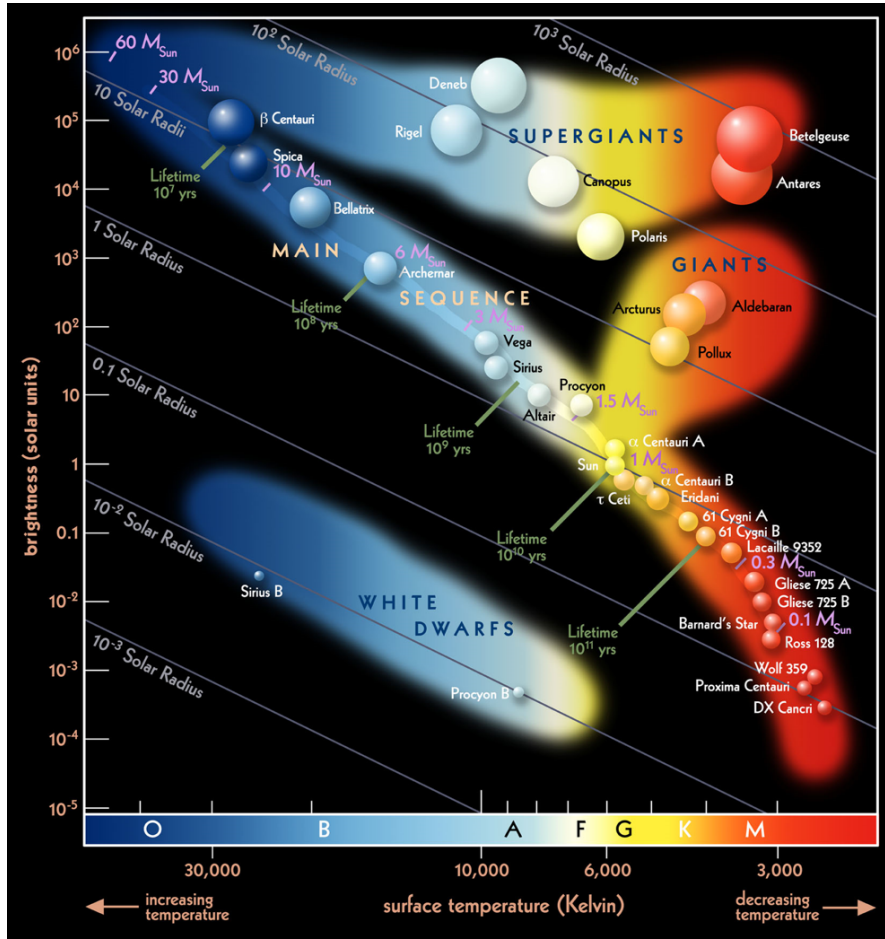


Figure 1.1: Hertzsprung Russel Diagram.¹

coolest stars (late type). Therefore, the effective temperature of a star can be derived from the luminosity equation, that is the energy per unit time over the surface and gives us the total power radiated by the star:

$$L = 4\pi R^2 \sigma T_{\text{eff}}^4, \quad (1.1)$$

where R is the radius, and T_{eff} is the effective temperature. For our Sun, the luminosity is $L_{\odot} = 3.86 \times 10^{26}$ W (Zeilik and Gregory, 1998, p. 201) and its absolute bolometric magnitude is $M_{\odot} = 4.74$, which indicates that the Sun is a fairly faint star (Stix, 2002, p. 6).

This is also anchored in its spectral class allocation, which ascribes the Sun the spectral class of a G2V star. From O to M stars, the temperature decreases, but the number of absorption lines increases. G stars have a temperature reaching from 6000 K (G0) to about 5100 K (G9) and contain singly ionised calcium, neutral metals, and have weaker hydrogen absorption lines. Furthermore, to express the degree of luminosity of the stars, luminosity classes have been introduced, where class I includes the most luminous stars and class V the main sequence stars, which then leads us to the Sun as a G2V star (Hanslmeier, 2002, p. 9). Being a G2V star with an effective temperature $T_{\odot}^{\text{eff}} = 5770$ K and a lifetime of 4.57×10^9 years (Stix, 2002, p. 24), the Sun lies on the main sequence of the HRD and sets the reference for other stars, in terms of brightness and radius. Over 90% of the stars near the solar system belong to the main

¹<https://www.eso.org/public/images/eso0728c/> [accessed 29 January 2016]

sequence, which is the phase in which they are most stable (Zeilik and Gregory, 1998, p. 262). What the stars on the main sequence also have in common is that they generate their energy from hydrogen burning in the core. Another very interesting finding was that stars spin up before they reach the main sequence (Bouvier *et al.*, 1986), and once on the main sequence their surface angular velocity decreases due to magnetic braking. At the moment, the Sun rotates with a surface velocity of only 2 km s^{-1} , whereas other stars can be 100 times faster, and will even slow down with age (Stix, 2002, p. 282).

Although the Sun is a star of average size, with $m = 1.99 \times 10^{30} \text{ kg}$ and a radius of $r_{\tau=2/3} = 6.96 \times 10^8 \text{ m}$ (Stix, 2002, p. 4), it still represents 99.97% of the solar system's mass (Lilensten and Bornarel, 2006, p. 7). The Sun consists by number of 93.96% Hydrogen, 5.91% Helium, and only 0.1% of heavy elements such as oxygen, carbon, nitrogen, silicon, magnesium, neon or iron (Hoyt and Schatten, 1997, p. 9). But, as has been mentioned and can be seen in the HRD, the Sun is a star of average properties, and there are other stars that have much higher or much lower temperatures, sizes, masses, and luminosities than the Sun. The good news of the Sun being an average star, or rather low-mass star, is that it will be on the main sequence for roughly another 4.5×10^9 years, as low-mass stars like our Sun evolve much slower than high-mass stars.

Furthermore, the evolutionary paths of stars differ significantly as a function of mass as well. First, to even start nuclear fusion in the core, it needs a temperature of about 10^6 K (Hanslmeier, 2002, p. 12). Then low-mass stars (with a mass lower than the Sun's) do not have enough mass to start helium burning. Thus, the star, after finishing hydrogen burning, collapses, and becomes a white dwarf. Stars of about one solar mass develop into red giants and later end up as white dwarfs. High-mass stars become supergiants and after the Helium burning, first in the core then in the shell, they burn carbon and finally produce iron. As the fusion of iron is an endothermic process and does not produce any energy, the star collapses. Eventually, according to their mass, stars either end up as a white dwarf, a neutron star, or a black hole. Very massive stars can end up as supernovae (Phillips, 1994, p. 28). Hence, in 4.5×10^9 years our Sun will become a red giant and finally a white dwarf (Hanslmeier, 2002, p. 8).

The Sun's properties like its temperature, mass, or size do not make it a very exotic star, but actually only an average out of trillions of stars. But from our point of view it is very special, as it is the closest star to us, and we can observe it in much more detail than any other star in the universe.

1.2 Continuous Radiation from Stars

What is actually visible from the Sun and enables us to observe it, is its energy flux, which is the energy per unit area per unit time received from the star. In the time of Hipparchus, around 150 BC, people divided the observed brightness of stars in magnitudes. The brightest star had the magnitude of $m = 1$, whereas the faintest was given a magnitude of $m = 6$. The Sun has an

apparent magnitude of $m_{\odot} = -26.74$, whereas the second closest star, Proxima Centauri, has an apparent magnitude of $m = 11.05$,² which is very faint and thus cannot be seen with the naked eye.

The colour of a star depends on its temperature, which can be deduced from its spectrum. The continuum can be described with the black body concept, as most of the stars can be approximated as black bodies and hence their emission by Planck's Law, given as a function of the frequency of electromagnetic radiation ν

$$I(\nu, T) = \frac{2h\nu^3}{c^2} \frac{1}{e^{\frac{h\nu}{k_B T}} - 1} \quad (1.2)$$

or as a function of the wavelength λ

$$I(\lambda, T) = \frac{2hc^2}{\lambda^5} \frac{1}{e^{\frac{hc}{\lambda k_B T}} - 1}. \quad (1.3)$$

The intensity of the radiation depends only on the temperature T , and hotter stars have their maximum intensity in the blue wavelength range and cooler stars in the red wavelength range. Adding up the intensity for all wavelengths gives us the total power emitted by a black body, which is given by the Stefan-Boltzmann law

$$F = \int_0^{\infty} B_{\lambda} d\lambda = \sigma T^4, \quad (1.4)$$

where σ is the Stefan-Boltzmann constant (Hanslmeier, 2002, p. 6). The wavelength at which the intensity is maximum is given by Wien's displacement law:

$$k = \lambda_{\max} T. \quad (1.5)$$

where k is Wien's displacement constant, λ the wavelength, and T the temperature.

1.3 Limb Darkening

When we look at the Sun, it seems brighter at the centre of the disc than at the limb. This effect is called limb darkening and evolves due to the increasing optical depth towards the limb and the temperature gradient from the centre up to higher layers.³

The optical depth τ is a term that describes the absorption of the incident radiation by a medium or gas at a certain wavelength. If $\tau = 1$, the incident radiation decreases to $1/e$, or 37% after it has passed the gas. Hence, τ depends on the composition of the medium, more precisely, on its chemical composition, temperature, and pressure prevailing (Weigert, Wendker, and Wisotzki, 2011, pp. 58). It is given by

$$\tau_{\nu} = \int \kappa_{\nu} dx, \quad (1.6)$$

²<http://www.astro.wisc.edu/dolan/constellations/extra/nearest.html>

³<http://astrowww.phys.uvic.ca/tatum/stellatm/atm6.pdf>

where κ is the opacity or the absorption coefficient of a medium (Weigert, Wendker, and Wisotzki, 2011, p. 58). For the Sun, it is the photosphere where the optical thickness is around unity. If we regard the optical thickness or depth as a distance, it becomes clear why there is limb darkening. The line from the solar surface to us (or the line-of-sight; LOS) gets larger at the limb, and thus the light that escapes from the photosphere has to travel a longer distance through the Sun's atmosphere towards the observer than that leaving the disc centre. On its (longer) way it gets absorbed and scattered more often, thus the light that reaches us from looking at the limb comes from higher and cooler layers.⁴

Geometrically, we consider the radiation to escape the Sun radially. Subsequently, the light that escapes from the centre of the Sun reaches the Earth with an angle of $\theta = 0^\circ$, whereas the angle gets bigger the more we look towards the limb and reaches $\theta = 90^\circ$ at the limb. The cosine of the heliocentric angle comes into account when calculating the intensity and consequently the intensity decreases towards the limb ($\cos 90^\circ = 0$). The Eddington approximation expresses the linear relation of the intensity variation with μ at $\tau = 0$, where $\mu = \cos \theta$:

$$\frac{I(0, \mu)}{I(0, 1)} = \frac{(2 + 3\mu)}{5}. \quad (1.7)$$

However, this approximation only works well for the central part of the solar disc, where we see deeper into the Sun, but not as good near the limb (Stix, 2002, p. 163).

Another phenomenon for which limb darkening is an indicator is the varying temperature and pressure throughout the solar atmosphere. If we now consider the LOS being the distance d from Earth to the Sun, we can see into deeper layers when we look at the disc centre, as the Sun is a sphere and hence the photosphere at the limb is further away. According to the Stefan-Boltzmann law, cooler gas radiates less energy per unit area than hotter gas. Connecting this to the phenomenon of limb darkening, we can conclude that at the disc centre the gas we see is hotter and therefore brighter, and at the limb the gas is cooler and less bright, and that the temperature throughout the photosphere decreases with height (Zeilik and Gregory, 1998, p. 203).

1.4 Radiative Transfer Theory and Spectral Lines

To examine and understand our Sun and other stars, the radiation that is sent off by stars is used in two ways. We measure the total intensity of the radiation and disperse the light to investigate it in detail (Zeilik and Gregory, 1998, p. 52). The assumption of Local Thermodynamic Equilibrium (LTE) is justified for most photospheric spectral lines. According to Stix (2002), in LTE

- there is no temperature gradient and the temperature T is constant,
- the particles follow the Maxwell distribution for their velocity,

⁴www.spektrum.de/lexikon/astronomie/randverdunklung/392

- the states of ionisation and excitation of the atoms are distributed according to the Saha and Boltzmann equations, respectively,
- the radiation field has the homogeneous and isotropic black-body form given by the Kirchhoff-Planck function, and
- we can simplify the radiative transfer problem using the Kirchhoff-Planck function as the source function in the radiative transfer equation: $S_\nu = B_\nu(T)$.

This means, given the temperature T only, the statistical particle velocities, the states of atoms in the gas, and the ratio of emission to absorption can be determined (Stix, 2002, p. 151). The following chapter shall give an explanation of how this light interacts with matter (radiative transfer theory) and therefore how spectral lines arise that help us understand the solar composition.

1.4.1 Radiative Transfer Theory

When light that is sent off from the Sun propagates through a medium, it can either be absorbed (and re-emitted) or scattered by atoms or ions, or it simply passes through the medium. Subsequently, the radiation changes its features like the intensity or its spectral distribution. The underlying theory of the transport of light through a medium (if the radiation keeps its direction of propagation) is named the radiative transfer theory (Weigert, Wendker, and Wisotzki, 2011, p. 58). There, the variation of intensity depends on the absorption and emission of the radiation by a medium and the total variation dI of the intensity I can be described by

$$dI_\nu = -I_\nu \kappa_\nu dx + \varepsilon_\nu dx, \quad (1.8)$$

then we get the differential equation for the radiation transfer

$$\frac{dI_\nu}{dx} = -I_\nu \kappa_\nu + \varepsilon_\nu, \quad (1.9)$$

or, by substituting $\kappa_\nu dx$ by $d\tau_\nu$ we get to

$$\frac{dI_\nu}{d\tau} = -I_\nu + \frac{\varepsilon_\nu}{\kappa_\nu}. \quad (1.10)$$

Implemented in Eqn. 1.10 is the source function $S_\nu = \frac{\varepsilon_\nu}{\kappa_\nu}$. Conveniently, in LTE, we can now apply Kirchhoff's law, which connects the source function with the Kirchhoff-Planck function insofar that we can substitute one by another (Stix, 2002, p. 26)

$$\frac{\varepsilon_\nu}{\kappa_\nu} = B_\nu(\nu, T), \quad (1.11)$$

If κ is known, we can assume the medium to act like a black body and the energy absorbed, is emitted following $\varepsilon_\nu = B_\nu(\nu, T) \kappa_\nu$. The solution for the radiative transport is then

$$I_\nu = -dI_{\nu,0} e^{-\tau_\nu^*} + \int B_\nu(\nu, T) e^{-\tau_\nu} d\tau_\nu \quad (1.12)$$

There, τ^* is the total optical thickness of the medium ($\tau_v^* = \int d\tau_v$) and $\tau^* \gg 1$ will lead to $e^{-\tau^*} \approx 0$. This means, the intensity of the radiation passing through a medium, which is optically thick for a certain frequency, is not dependent on the initial intensity, but only on the temperature distribution in the medium (Weigert, Wendker, and Wisotzki, 2011, p. 60). We can, again, say that the absorption and emission of photons originating in the solar photosphere depend strongly on the composition and temperature of the medium.

1.4.2 Spectral Lines and Line Broadening

If we now investigate the spectrum of the radiation, we can draw conclusions about the solar atmosphere, where the incident photons originate. For the collision of particles, we consider a Bohr atom and the quantum nature of light, which is light consisting of photons. The atom consists of a nucleus containing protons and neutrons, surrounded by electrons in discrete orbits. Being in one of those orbits the electron does not radiate. It only emits or absorbs radiation or photons when the electron jumps from one orbit to another, where the energy of the photon equals the energy difference between the orbits. This means, if an electron makes a transition from a higher orbit (or a higher excitation state) to a lower orbit, it emits radiation in the form of a photon (Zeilik and Gregory, 1998, p. 160)

$$E(n_a) = E(n_b) + h\nu, \quad (1.13)$$

where $n_a > n_b$. This is called a radiative excitation, whereas the excitation rising from an atom colliding with a free particle, either another atom or an electron, is called collisional excitation (Zeilik and Gregory, 1998, p. 162). However, if the electron makes a transition from a lower to an upper orbit, it has to absorb a photon with the energy of exactly the energy difference between the orbits beforehand

$$E(n_b) + h\nu = E(n_a). \quad (1.14)$$

Those absorptions and emissions lead to changes in the continuum and we see either emission or absorption lines as either bright or dark lines in the spectrum. As the energy difference from one orbit to another changes from atom to atom, the absorption or emission lines change and are therefore indicators for a certain chemical element or molecule. The lowest orbit is called the ground state ($n = 1$) and is most strongly bound to the nucleus. The energy for each orbit can be calculated with (Zeilik and Gregory, 1998, p. 160)

$$E(n) = \frac{-(2\pi^2 m e^4 k^2 Z^2)}{n^2 h^2}. \quad (1.15)$$

For simple atoms like the Hydrogen atom we can assume the atom is a Bohr atom, comprised of a nucleus with the electron orbiting around it. In fact, if we had an atom with more electrons, we would need to take quantum-mechanical theories into account (Zeilik and Gregory, 1998, p. 161).

The spectral lines that come into being as a result of the transitions from one orbit to another have two main characteristics: one is the intensity of the line and the other the width. The intensity of an absorption or emission line is proportional to the amount of photons that were absorbed or emitted during a transition. Furthermore, the line is never a sharp line but has a profile, where the intensity of the profile varies with wavelength (Zeilik and Gregory, 1998, p. 166). Hence, if we talk about a spectral line at a certain wavelength, we rather mean a wavelength band or range. Plotting this spectral line and its course of intensity, we get its profile as a curve with an area A . This profile can be illustrated by a rectangle of the same area A , where the width of this rectangle is called the “equivalent width” and the height of the rectangle represents the height of the continuum. The equivalent width is an indicator for the strength of the line, which depends on its intensity and width. If a line has become saturated, meaning the intensity of an absorption line reaches zero intensity, the equivalent width can only increase by the increase of the wings. The spectral line broadening is mainly the result of: (1) natural broadening, (2) thermal Doppler broadening, (3) collisional broadening, and (4) Zeeman effect, if the line is sensitive to the magnetic field.

The reason why a line is never sharp but has a minimum width is the *natural broadening*, which has its explanations in quantum mechanics (Zeilik and Gregory, 1998, p. 169). The wave-particle duality gives all atomic particles both a particle and a wave nature. This means that an electron in an atom has a wave nature, too. According to the Heisenberg uncertainty principle, the energy of an electron of a given state is

$$\Delta E = (1/2\pi)(h/\Delta t), \quad (1.16)$$

where h is Planck’s constant and Δt the lifetime of the state, before it decays. This equation relates the energy of a certain state to the lifetime in that state before the atomic state decays. Meaning if the lifetime in that state is short, the energy uncertainty is large. A short life time leads to a high energy uncertainty and therefore to an unsharp frequency. If this state (with the uncertain energy) decays, it releases the energy, where the released energy changes slightly. This energy has its peak in the theoretical / average energy of this state, but the actual energy that is released varies, which is why the line is not sharp but broadened (Weigert, Wendker, and Wisotzki, 2011, p. 54). The lifetime of an atomic state is 10^{-8} s before it decays, whereas a ground-state can last forever (Zeilik and Gregory, 1998, p. 169). An electron leaves its excited state coincidentally, and its lifetime can only be stated statistically with the so-called transition probability or the mean lifetime (Weigert, Wendker, and Wisotzki, 2011, p. 54).

Thermal or Doppler broadening depends on the composition and temperature of the gas, but also on the direction towards the observer. If an absorbing gas particle is moving towards the observer, the radiation it emits is blue-shifted (shifted to shorter wavelengths). If the gas particle is moving away, it will emit red-shifted radiation. Conventionally, if a source moves away from the observer, then $v > 0$, and if the source is moving towards the observer, then $v < 0$. In

any case, in LTE, the velocity of a gas particle at a temperature T follows the Maxwellian distribution, where the *most probable* speed is given by (Zeilik and Gregory, 1998, p. 169)

$$v_p = \sqrt{\frac{2kT}{m}}. \quad (1.17)$$

This equation indicates that heavier particles move more slowly than lighter particles. The following equation connects the speed of a particle with the according Doppler line broadening (Weigert, Wendker, and Wisotzki, 2011, p. 61)

$$\frac{\Delta\lambda}{\lambda_0} = \frac{\lambda - \lambda_0}{\lambda_0} = \frac{v_r}{c}, \quad \text{and} \quad \frac{\Delta\nu}{\nu} = \frac{\nu_0 - \nu}{\nu} = \frac{v_r}{c}. \quad (1.18)$$

Here λ is the measured wavelength, λ_0 is the wavelength at rest, and $v_r \ll c$. Consequently, because of their lower speed, heavy particles produce a narrower line width than lighter particles that move faster at a given temperature and therefore result in wider lines. The line width and the average velocity are proportional to \sqrt{T} (Weigert, Wendker, and Wisotzki, 2011, p. 194). Thus, one can say the lighter the particle, the broad the line at a given temperature and the higher the temperature the larger the line width as well. That means, from the Doppler broadening we can deduce the movement of a particle and its velocity (Weigert, Wendker, and Wisotzki, 2011, p. 61).

The *collisional or pressure broadening* is the broadening of a line because of neighbouring, charged particles and therefore depends on the density or pressure of the gas as well (Zeilik and Gregory, 1998, p. 170). The electron's or ion's electrical field can perturb the energy level of an atom and therefore influences the transition between the levels (Mullan, 2010, p. 53). If it perturbs an emission or absorption process, the line gets broadened (Weigert, Wendker, and Wisotzki, 2011, p. 193). The line broadening or shifting resulting from the electric field of charged particles is called the Stark Effect (Mullan, 2010, p. 53), i.e., the higher the gas density and pressure the larger the line width (Zeilik and Gregory, 1998, p. 170).

The broadening of a spectral line due to the *Zeeman effect* is not an actual broadening but a splitting of the line because of the electron's dipole moment. What happens when the atom is placed in a magnetic field is the separation of the energy levels of an atom into three or more sublevels (Zeilik and Gregory, 1998, p. 170). The lines are very narrow and close to each other, so that we only see a broadened spectral line, if the resolution is not high enough and the magnetic field is not too strong. However, with a high resolution or a strong magnetic field, we can see the splitted line and can draw conclusions about the magnetic field strength and the direction of the field lines (Zeilik and Gregory, 1998, p. 170).

The different reasons for spectral line broadening lead to different shapes of the line as well. We will now consider absorption lines of bound-bound transitions and their profile. If the particles of a gas follow the Maxwellian distribution for their velocity, the profile of a line

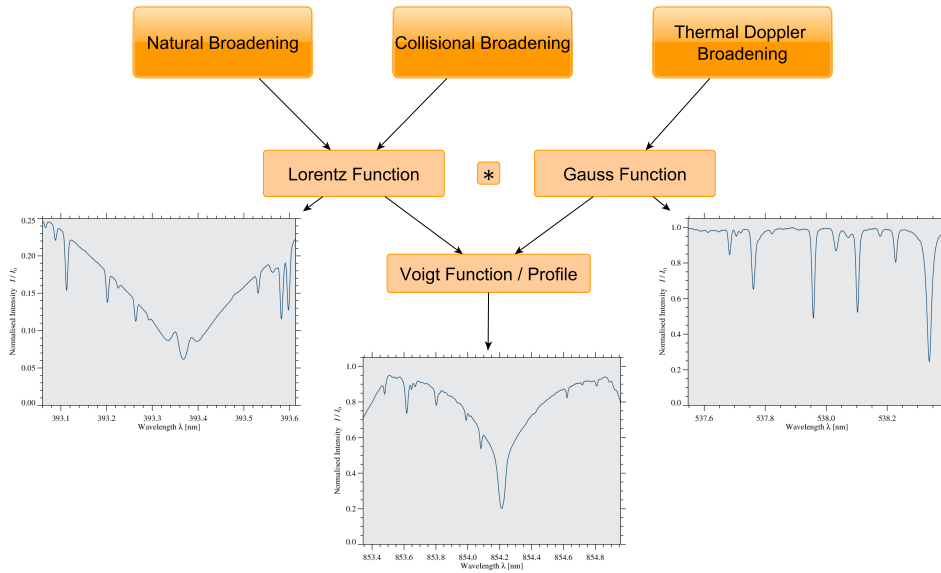


Figure 1.2: This scheme depicts how the shape of a line profile can be allocated to the reason for the line broadening. Natural broadening and collisional broadening lead to a Lorentzian profile (example on the left: Ca II K) and Doppler broadening to a Gaussian profile (example on the right: C I). In general, natural and collisional broadening act together and we obtain a Voigt profile, for which the Ca II in the infrared is an example of (middle graph).

broadened due to the Doppler effect shows a Gaussian profile (Mullan, 2010, p. 52) that is described by (Stix, 2002, p. 47)

$$\phi_D(\Delta\nu) = \frac{1}{\sqrt{\pi}\Delta\nu_D} \exp[-(\Delta\nu/\Delta\nu_D)^2]. \quad (1.19)$$

If a line, however, gets broadened due to collisional effects, it can be described by the Lorentzian profile (Stix, 2002, p. 47)

$$\phi_C(\Delta\nu) = \frac{\gamma}{(2\pi\Delta\nu)^2 + \gamma^2/4}. \quad (1.20)$$

Here, $\phi(\nu)$ is the normalised shape function of the line or the line profile, $\Delta\nu = \nu - \nu_0$ is the difference of the frequency to the frequency in the line core and γ is the constant of collisional damping (Stix, 2002, p. 48). In the core of the lines the Doppler profile dominates the shape of the line, whereas the wings can be better expressed by “the slowly decaying damping profile” due to the different height in which the different parts of the lines emerge and composition of the gas prevailing there. But usually, the lines are broadened due to various effects (Doppler and collisional broadening) so that the shape does neither show a purely Gaussian nor a purely Lorentzian function. Those profiles require the convolution of the Gauss and the Lorentz functions, and we get the Voigt function to describe the shape of our spectral lines. The Voigt function is given by (Stix, 2002, p. 153):

$$H(a, \nu) = \frac{a}{\pi} \int_{-\infty}^{\infty} \frac{e^{-y^2}}{(\nu - y)^2 + a^2} dy. \quad (1.21)$$

The Fig. 1.2 illustrates which cause for the broadening leads to which profile of the spectral line.

Chapter 2

The Sun

2.1 Sun-as-a-Star Observations

The Sun is the closest star to Earth, which is why it can be observed in more detail compared to other stars. Hence, it plays an important role as a source of precise astrophysical information which can, in return, help us understand many other stars.

Individual surface features of the Sun such as sunspots or solar flares can be observed directly, whereas for other stars such properties have to be derived indirectly from variations of star-integrated spectral line profiles or luminosity measurements. With solar disc-resolved and solar disc-integrated observations, the contribution of individual features to the whole Sun-as-a-star spectrum can be investigated. In addition, by making a connection between properties of disc-resolved images and disc-integrated (or Sun-as-a-star) spectra solar data is useful to interpret stellar spectra. Apart from comparisons with observations of other stars and stellar activity, Sun-as-a-star observations are mainly employed for studies of solar activity cycles, solar (differential) rotation, and long-term variations in properties of the mean chromosphere.

Chromospheric spectral lines such as Ca II K & H are the basis for disc-integrated indices that serve as proxies for the total magnetic flux and the solar chromospheric activity. They also allow us to study long-term variations in solar irradiance and their effects on the climate on Earth (Pevtsov, Bertello, and Marble, 2014). In the HRD, the Sun resides in the mid-range of the main sequence, according to its spectral type. This means that the Sun is a G star with a surface temperature of 5770 K, and is currently in the stable phase of hydrogen burning.

2.2 Solar Structure

The Sun is mainly composed of hydrogen (by number of atoms 94%), helium (6%), and only 0.1% other elements (Kutner, 2003, p. 101). It generates its energy in its core, above which the radiative zone and the convection zone lie (Zirker, 2001, p. 10). Radiation transport happens in the entire Sun. Whereas most radiation of the solar interior is absorbed before it arrives

at the surface, we can see the net effect of radiation escaping at the surface, the photosphere. Consequently, the visible light from the Sun originates in the photosphere (the bottom layer of the solar atmosphere), which is followed by the chromosphere and the transition region. The outermost layer is the corona, which extends far into space.

2.2.1 Solar Interior

The Sun's interior cannot be directly observed, as all photons that escape the Sun are of photospheric origin. For this reason, theorists developed models to explain what happens in the solar interior. Nowadays, helioseismology offers opportunities to observe the interior indirectly and compare it to the theory with almost matching results. The Sun's core encompasses roughly one quarter of its radius. Through hydrogen burning, where the hydrogen converts into helium, energy is released. As the temperature outside the core is not sufficiently high to ignite hydrogen burning, the core is the only source of all the energy that the Sun ever produces (Zirker, 2001, p. 36). The energy leaves the core, mainly as γ -rays and X-rays, and then passes through the radiative zone. This zone received its name because the energy transfer in this region happens through radiative processes, in fact via photons. The photons are scattered, absorbed, and re-radiated, whereas this process can take several million years (Haigh, Lockwood, and Giampapa, 2004, p. 111). The radiative zone is in hydrostatic equilibrium, which means that the temperature, pressure, and density of the plasma are steady, so that there is a balance between pressure and gravity. The tachocline is the boundary between the radiative zone and the convection zone, where the rotation changes from a solid body rotation to differential rotation, which is why it is also known as the shear layer (Haigh, Lockwood, and Giampapa, 2004, p. 117).

The convection zone is the very dynamic, 200 000 km thick zone that brings the energy up to the surface. Hot streams of gas undergo updrafts and as they cool, downdrafts, and thus circulate the hot plasma. The updrafts occur on different spatial scales: supergranules can be up to 30 Mm across, mesogranules up to 5 Mm across, and granules just a few thousand kilometers across. These convective patterns are well-ordered, uniform, and isotropic, whereas smaller circulations of plasma can move very chaotically (Zirker, 2001).

2.2.2 Solar Atmosphere

Strictly speaking, the Sun does not have a surface, but if it had one, it would be the few hundred kilometre thick and almost 6000 K hot *photosphere*, as this is the densest layer of the atmosphere and the layer where the radiation finally escapes (Zirker, 2001, p. 102). However, the surface is not smooth but has a structure called granulation, which is the result of the overshooting convection in the solar interior. Granules are bright areas of about 1400 km diameter with a dark surrounding. They evolve when hot gas from the convection zone circulates and rises, which is the bright part of the granules and as the gas cools, it sinks down, which can be seen in the dark edges of the granules (Kutner, 2003, p. 105). Furthermore, when we look at the Sun,

its centre appears brighter than towards the limb, which is termed limb darkening, as discussed in Sect. 1.3 (Zeilik and Gregory, 1998, p. 202).

Features of the photosphere and indicators for an existing magnetic field are sunspots and faculae. Sunspots appear as dark spots on the solar surface as they inhibit the upflow of the energy from below because of their strong magnetic field. They have very dark umbrae surrounded by less dark penumbrae. The temperature of an umbra is about 3800 K and the magnetic field strength is about 0.15–0.35 Tesla, which is roughly 1000 times larger than the average magnetic field of the quiet Sun. Umbrae and penumbrae can have typical diameters of 20 Mm and 40 Mm, respectively. Sunspots usually form in groups, where one sunspot is paired with another or with additional spots in a bipolar magnetic region. Sunspots have a lifetime of several days to several months, mainly depending on their size (Haigh, Lockwood, and Giampapa, 2004, p. 124).

Faculae are features with a high magnetic field strength as well. In contrast to sunspots, they are bright, considerably smaller, but much more numerous and hence cover a bigger area. They can be better observed near the limb, where their contrast with respect to the quiet Sun is greater. Because of their small size the radiation from the walls of the faculae can maintain the temperature in the tube. As the magnetic field B is greater, the gas pressure inside the tube has to be smaller than outside due to

$$P_{\text{total}}^{\text{out}} = P_{\text{total}}^{\text{in}} \quad (2.1)$$

$$P_{\text{total}}^{\text{out}} = P_B + P_{\text{gas}}^{\text{in}}. \quad (2.2)$$

Hence, as the temperature stays the same, the density of the gas must decrease, which leads to a smaller opacity compared to the surrounding area. That means we can see deeper into the Sun, where it is hotter, which is why faculae seem brighter (Haigh, Lockwood, and Giampapa, 2004, p. 205). Faculae usually occur near sunspots or sunspot groups and their number increases and decreases with the number of sunspots. They can be observed in various wavelengths, in the photosphere and the chromosphere, whereas their cross-section increases with height, and they form so called plages that can be seen in the chromosphere (Haigh, Lockwood, and Giampapa, 2004, p. 132).

The *chromosphere* is the roughly 10 Mm thick layer following the photosphere. The chromospheric temperature is about 4000–30 000 K, but the reason why Sun does not appear as hot is that the chromosphere is an optically thin medium, thus it does not contribute much to the total radiation of the Sun (Kutner, 2003, p. 109). The chromosphere can only be seen, if the light of the photosphere is blocked out, for example, during a solar eclipse. It then appears red because of the dominant $H\alpha$ emission of the Balmer series. Because the gas is optically thick for the wavelength range of this line, we can best study the chromosphere in this particular line (Zeilik and Gregory, 1998, p. 207).

Moreover, in the chromosphere one can see manifestations of larger-scale convection, i.e., signatures of the supergranulation as a network of bright points, which is particularly prominent in the Ca II H & K lines. Other features of the chromosphere are dark mottles on the solar disc that are related to spicules that can be seen at the limb. The dark mottles form a network that follows the supergranular pattern as well. As the boundaries of supergranules are related to concentrated magnetic flux and thus seem dark in H α , the mottles probably also exist due to a local enhanced magnetic field. On average spicules have a height of 5000 km, a width of up to 500 km, a temperature of 8 000 – 10 000 K, and velocities of 20 km s⁻¹. Apart from that, not much is known about spicules, how they form and how their mass flux returns to the solar surface (De Pontieu, Erdélyi, and James, 2004).

Another effect that is notable in the chromosphere is the increasing temperature with height, which leads to emission reversals. That is, within an absorption line, one can see emission around the line core. As we see increasing absorption of a line, we see into higher layers of the atmosphere, as more and more photons are absorbed on their way. As long as the temperature decreases (hence the density of gas increases) with height the absorption line becomes darker and darker, as – again – more photons of this particular energy are absorbed. At some point the absorption becomes so strong and the line so dark that we can see emission from higher layers, meaning we can see emission lines that actually originate in higher, hotter layers of the chromosphere above the temperature minimum region. The chromospheric heating is related to a stronger magnetic field. Therefore, chromospheric emission lines are related to the magnetic field strength (Stix, 2002, p. 389).

The *transition region* is the region between the 10⁴ K hot chromosphere and the million-degree hot corona. The temperature of these two regions differs by a factor of 100, where the increase happens rapidly. The transition region is also characterised by its extreme spatial inhomogeneity. As a result, it undergoes a massive discontinuity in temperature and pressure. It is best observed in space at the extreme ultraviolet (EUV) spectral range from 50–160 nm. As certain highly ionised atoms form only at certain temperatures, observations of the transition region reveal emission lines and show that it contains numerous different species of ions (Stix, 2002, p. 392).

The *corona* is the faintest layer of the solar atmosphere, which can only be seen during a solar eclipse, when the photosphere is covered by the moon (Kutner, 2003, p. 110). At these times, we can also see that the corona does not at all have a clear edge but reaches far into space into the heliosphere, the region in space that is dominated by the solar wind outflow of ionised gas and a weak magnetic field (Haigh, Lockwood, and Giampapa, 2004, p. 111). The visible corona can be divided into the K-corona (referring to the German word Kontinuum) and the F-corona (named after the German optician and physicist Joseph von Fraunhofer). They mainly differ in the fact that in the F-corona (dominating near the Sun) one can see absorption

lines like in the photospheric continuum, whereas there are no absorption lines in the K-corona, further out up to a few solar radii (Zeilik and Gregory, 1998). The corona's high temperature, about 2×10^6 K, ionises the gas, whereas the low density makes recombination a rare process. As collisions depend on the density, the temperature in the corona is relatively stable, as the density there is very low. But the main question is, how the corona heats up to such high temperatures, given that the corona is so far away from the core, which is its energy source (Kutner, 2003, p. 110).

2.3 Solar Cycle

The solar cycle exhibits an 11-year long, periodic change of the solar activity, caused by the change of the Sun's magnetic field. The cycles are all individual, and differ among others in their maxima and minima, their shapes, and their periods (Hathaway, 2010). The mere fact that the Sun is active, i.e., it goes through non-stationary processes in contrast to the quiet Sun, led to the conclusion that there must be a convection zone and a corona (Usoskin, 2013). Indices of solar activity can be divided into physical (meaning directly measurable indices), or synthetic (meaning calculated by using observed phenomena or data and a certain algorithm). Furthermore, these indices can be again divided into direct indices (directly relating to the Sun) or indirect indices (inferred through effects that were caused by the solar activity). In the following, I will concentrate on the sunspot number and the solar irradiance as indices for solar activity or the solar cycle. Only if we understand the behaviour of solar radiation and its variability, we can, for example, tell how substantial mankind's contribution is to climate change.

2.3.1 Sunspot Number

Sunspots are features on the Sun that have been observed for the longest time. Actual recordings exist from China, ranging back 2000 years, whereas in the western countries sunspots were observed with the advent of telescopes in the 17th century. Nowadays, the International Sunspot Number (ISN) is the most essential indicator for solar activity, because of the long-term record and its close correlation with the rise and fall of solar activity (Hathaway, 2010). Hence, when the Sun is more active one can see more sunspots but at the same time the Sun appears brighter on average, as dark sunspots and bright faculae are related and appear in tandem (Solanki and Unruh, 2013). Note that we investigate not just the number of sunspots throughout the solar cycle, but also their positions; we can see in Fig. 2.1 that sunspots appear in both hemispheres. At the beginning of a solar cycle, there is an increased number of sunspots in high latitudes above $20-25^\circ$. During the 11-year cycle they appear ever closer towards the equator (Hathaway, 2010).

¹<http://solarscience.msfc.nasa.gov/SunspotCycle.shtml> [accessed 26 January 2016]

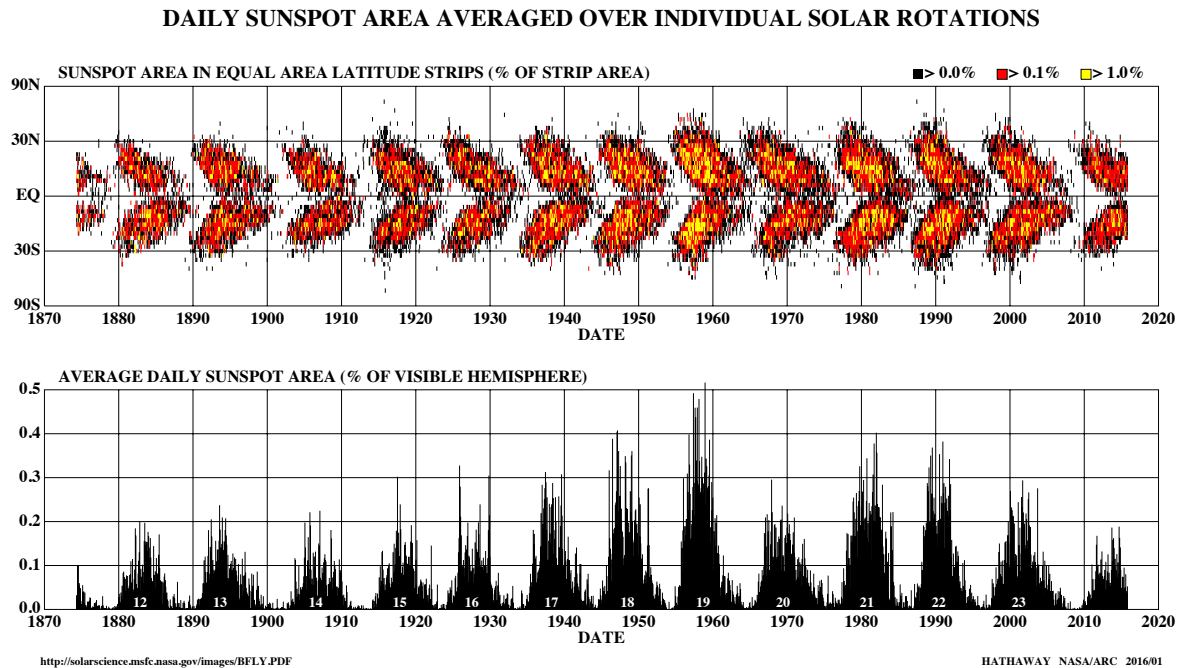


Figure 2.1: The butterfly diagram (*top*) shows the latitude dependence of sunspots over the solar cycle. The average daily sunspot area (*bottom*) is closely correlated with the sunspot number and indicates the strength of the solar cycle (Hathaway, 2010).¹

2.3.2 Solar Irradiance

Solar irradiance is a spectral quantity (also known as solar spectral irradiance (SSI)), meaning the measured irradiance depends on the referred wavelength range. Total solar irradiance (TSI), however, is the integrated spectral irradiance and describes the amount of total electromagnetic radiation emitted by the Sun over all wavelengths that crosses a square metre per second and is measured just above the Earth's atmosphere. The TSI was long thought to be constant but in actuality it changes slightly (Hathaway, 2010). Solar irradiance changes on all times scales, whereas this present study deals with the diurnal time scale over the 11-year solar cycle. The solar irradiance variability is also found to depend strongly on the wavelength; for example, although the TSI changes about 0.1% over the solar cycle, we find the SSI can change in the ultraviolet (UV) up to 100% (Krivova, Solanki, and Floyd, 2006). This is due to the change of the magnetic field and therefore the number of sunspots and faculae that contribute to the Sun's atmospheric temperature structure and hence to the production of UV photons.

Measuring the emitted radiation of the Sun over a long time, would obviously be the best way to investigate solar irradiance variability. But in fact, apart from the high costs of space

missions, it is very difficult to get accurate measurements from space, due to the degradation of the instruments with time, which means the sensitivity of the detectors of the instruments diminishes over time ([Solanki and Unruh, 2013](#)). In addition, calibrating UV photometers and spectrometers has proved to be a formidable task.

Chapter 3

Chromospheric Features

The reason why the solar surface is not uniform, but shows structures that vary over time is related to the varying magnetic field. It is also reason for the presence of a chromosphere. The chromosphere is optically thick for the radiation at the wavelengths of the strong chromospheric absorption lines $H\alpha$ and $Ca\ II\ H\ \&\ K$, which means that the light coming from the photosphere does not pass the chromosphere at those wavelength ranges. This implies that studying those lines leads us to a better understanding of the chromosphere itself.

$H\alpha$ is an emission line of the Balmer series, which describes the transition of an electron from any state $n > 2$ to the orbit of $n = 2$, whereas for $H\alpha$ the transition is from $n = 3$ to $n = 2$ (Zeilik and Gregory, 1998, p. 170). The Balmer lines originate in the chromosphere due to the specific temperature required for hydrogen to be in an excited state with $n \gg 2$ and this temperature is found in the chromosphere, where collisions for the excitation occur more often. Observing the Sun in $H\alpha$ we can see dark and bright structures like the so-called chromospheric network, filaments, plages, prominences, mottles, and spicules. The chromospheric network, as can be seen in Fig. 3.1, covers the whole solar disc and makes the photospheric supergranulation pattern visible (Zeilik and Gregory, 1998, p. 208).¹

The bright patches that we can see are plages, and the dark, elongated ones are filaments as shown in Fig. 3.1. In contrast to the bright parts of the network, plages are even brighter and only appear occasionally, as they are remnants of decaying active regions. Filaments appear dark, as they contain cooler plasma. They evolve because of dense clouds of material that are suspended by loops of magnetic field above the solar surface.¹ At the limb where they are visible against the dark background of the universe, filaments appear bright as shown in Fig. 3.2 and are often referred to as prominences, where both are fundamentally the same (Mackay *et al.*, 2010). Filaments usually occur between different polarities of the solar magnetic field. They can be classified as active regions filaments, intermediate filaments, and quiescent filaments, where it should be mentioned that these descriptive terms only refer to the state of the magnetic field that underlies the structure. Being related to the activity of the magnetic field, the active

¹<http://solarscience.msfc.nasa.gov/feature2.shtml>

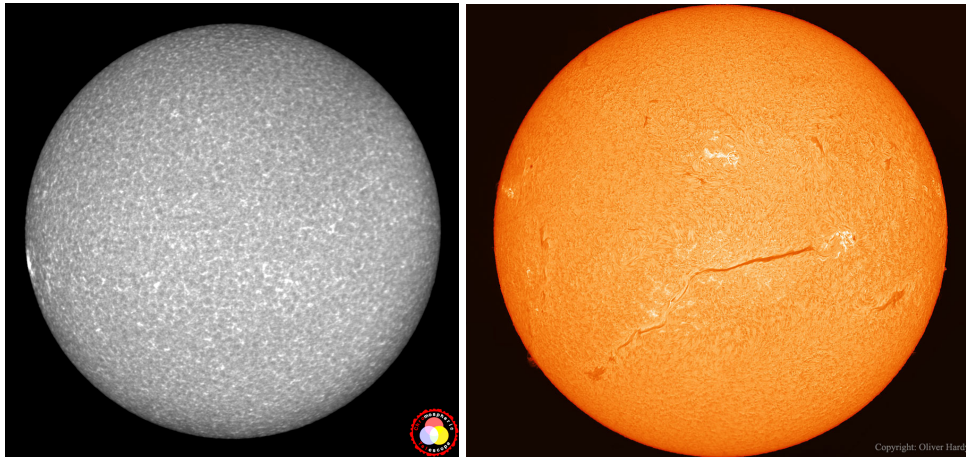


Figure 3.1: The image of the Sun in Ca II K obtained with the Chromospheric Telescope (ChroTel, [Bethge et al., 2011](#)), shows the chromospheric network that is distributed over the entire solar disc and reveals the supergranular pattern (*left*).³ The long dark structures that can be seen in the H α image (*right*) are filaments and the bright batches that occur here and there are plages.⁴

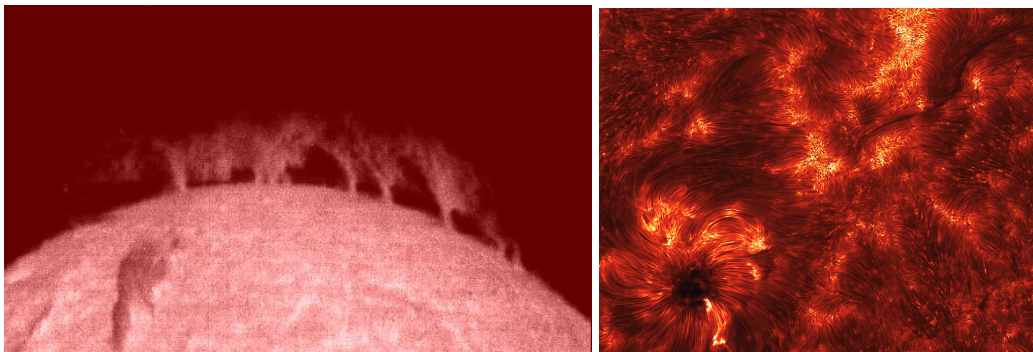


Figure 3.2: This image shows chromospheric prominences⁴ seen at the solar limb and unveil the gas that is trapped in loops of magnetic field (*left*) and the “Astronomy Picture of the Day” on 2010 November 2 showing high resolution disc counterparts spicules (*right*).⁵

and intermediate filaments occur within the sunspot belts and the quiescent filaments can be located anywhere on the solar disc.

Decaying sunspots dissolve into small-scale brightenings, i.e., plages. Plages and filaments are, therefore, connected to solar activity as well ([Zeilik and Gregory, 1998](#), p. 208). The so-called active regions are large areas with strong concentrations of magnetic fields around sunspots. Another type of small-scale chromospheric features are mottles. In the line wings of H α we can see dark mottles, or spicules when arising at the limb ([Stix, 2002](#), p. 388). These dark mottles form a network, which follows the supergranulation pattern. The astonishing aspects of spicules are their size, temperature, and density. Macrospicules are 20 000 km high and reach a velocity of 25 km s⁻¹ ([Stix, 2002](#), p. 388). A good overview of features of the Sun in each atmospheric layer can be found in the online open-access journal “Living Reviews in Solar Physics”.²

²<http://spie.org/newsroom/technical-articles-archive/11-1200/1260-chrotel-a-new-robotic-solar-telescope> [accessed 19 January 2016]

³<http://apod.nasa.gov/apod/ap150210.html> [accessed 19 January 2016]

⁴<http://solarscience.msfc.nasa.gov> [accessed 19 January 2016]

⁵<http://apod.nasa.gov/apod/ap101102.html> [accessed 19 January 2016]

²<http://solarphysics.livingreviews.org/>

Chapter 4

Integrated Sunlight Spectrometer

Modern synoptic observations of the Sun began in the late 1950s / early 1960s and included visual and/or photographic data taken in the $H\alpha$ and Ca II K line (Balasubramaniam and Pevtsov, 2011). There are currently three major programmes existing to observe the Sun as one would observe other stars. Beside the Ca II K line monitoring program at Sacramento Peak (Keil, Henry, and Fleck, 1998) and the Solar-Stellar Spectrograph at Mt. Wilson Observatory (Wilson, 1978), there is the Integrated Sunlight Spectrometer (ISS), which is part of the Synoptic Optical Long-term Investigations of the Sun (SOLIS, Pevtsov, Bertello, and Marble, 2014) programme. Since space missions are expensive, relatively short-lived, inflexible, and susceptible to operational problems, SOLIS is located at the Kitt Peak National Observatory (KPNO) in Arizona, on top of the former Kitt Peak Vacuum Telescope. However, after spending a decade there, it moved in 2014 to the “GONG farm” in Tucson, and will soon be relocated once again at the end of 2016.¹ SOLIS is funded by the National Science Foundation (NSF) and designed / built by the National Solar Observatory (NSO).² SOLIS replaced NSO’s older synoptic observing facilities with a state-of-art instrument suite. It provides optical observations of the Sun on a continuous basis over the time scale of minutes to decades for several decades. Spatial scales range from 1 Mm to the full disc and corona (Keller, 1998).

According to Balasubramaniam and Pevtsov (2011), the SOLIS programme is designed to address three major questions:

1. What causes the solar cycle?
2. How is energy stored and released in the solar atmosphere?
3. How do the solar radiative and non-radiative outputs vary in time?

Therefore, it is meant to help understand long-term changes in solar activity that include the solar dynamo that produces the solar activity cycle, sudden energy releases in the solar atmosphere, and solar irradiance changes and their connection to global change.² One of the

¹<http://solis.nso.edu/0/news/news.html>

²<http://solis.nso.edu/0/info/aboutsolis.html>

Table 4.1: Nine spectral bands measured by ISS with λ_0 being the centre of each spectral band, $\delta\lambda$ the bandwidth and $d\lambda/dx$ the average linear dispersion over time (see Table 1 in Bertello *et al.* (2011)).

Type	λ_0 , nm	$\Delta\lambda$, nm	$d\lambda/dx$, pm/pixel	Start date
CN band	388.40	0.58	0.564	December 4, 2006
Ca II K	393.37	0.55	0.541	December 1, 2006
Ca II H	396.85	0.53	0.522	December 4, 2006
C I	538.00	0.84	0.824	December 4, 2006
C I (with iodine lines)	538.00	0.84	0.824	January 7, 2008
Mn I	539.41	0.83	0.816	December 4, 2006
H-alpha	656.30	1.14	1.12	August 31, 2007
Ca II	854.19	1.61	1.58	December 13, 2006
He I	1083.02	1.65	1.61	December 4, 2006
NaD1	589.59	0.98	0.956	March 23, 2011

operational goals is to produce real-time and near real-time data for forecasting space weather and to improve scientific achievements of space missions and ground-based projects (Keller, 1998). The data are also useful to predict terrestrial changes that have an impact on us in many respects, for example, power and communication interruptions, increased radiation exposure at high altitudes, or degradation of navigation accuracy (Keller, Harvey, and Giampapa, 2003). SOLIS and its instruments aim for better and more efficient observations and to enhance the quality and quantity of data at lower operating costs. To achieve this, different kinds of observations, and hence different instruments, are needed. Over time, SOLIS has been upgraded and the observatory, as it is now, consists of three instruments:

- the Vector Spectromagnetograph (VSM),
- the Full Disk Patrol (FDP), and
- the Integrated Sunlight Spectrometer (ISS).

In the following I will explain each of these instruments: VSM/FDP will only be discussed briefly, whilst I focus more attention on ISS due to the use of its data in this thesis.

The Vector Spectromagnetograph (VSM) was developed to obtain high-quality magnetic field observations in the photosphere and the chromosphere. Therefore, the VSM can take full-disc magnetograms by scanning the solar image, which is achieved by moving the telescope in declination. In addition to that, it can take a series of area scans by scanning a portion of the solar disc. Every day, the VSM mainly observes photospheric full-disc vector-magnetograms, chromospheric and photospheric full-disc magnetograms, and also full disc He I 1083.0 nm line characteristics.³

The Full Disk Patrol (FDP) is a full-disc imager that uses tunable Lyot filters and a 2048×2048-pixel CCD camera (about 1'' pixel⁻¹ image scale). It takes observations with high temporal

³<http://solis.nso.edu/0/info/aboutsolis.html>



Figure 4.1: The Integrated Sunlight Spectrometer (ISS) installed at the Kitt Peak SOLIS Tower, was relocated after 10 years, in 2014, to the “GONG farm” in Tucson.⁴ The light is fed into the instrument via optical fibers (left).⁵

cadence (about 10 s) in spectral lines such as $H\alpha$, $Ca\ II\ K$, $He\ I$, continuum (white light), and photospheric lines. In addition, Doppler velocity maps can be derived from narrow-band filtergrams. Since the patrol telescope has been integrated into SOLIS in June 2011, it has taken observations in test mode. It will eventually provide imaging data for space-weather forecasting. This will help understand triggering and evolution of solar flares and coronal mass ejections, and it will also complement space-based X-ray and EUV observations.

The Integrated Sunlight Spectrometer (ISS) has been operating since December 2006 and is designed to take both high ($R = 300\,000$) and moderate ($R = 30\,000$) spectral resolution observations of the Sun every day. It records variations exhibited by the spatially unresolved Sun as manifested in several important spectral windows. The key parameters are observed in nine spectral bands that are listed in Table 4.1, even though it could be tuned to any wavelength in its wavelength range of 350–1100 nm (Bertello *et al.*, 2011). The measurements in these bands are used to study changes in the solar irradiance along the solar cycle and to measure the response of different layers of the solar atmosphere to the magnetic activity of the Sun. ISS observations are also employed to interpret and calibrate stellar measurements in terms of stellar activity and cycles.

Scrambling the sunlight within this broad wavelength range is important to accurately measure integrated sunlight. To improve this scrambling, an 8-millimetre lens focuses a 400-micrometre diameter image of the Sun on the input face of a 600-micrometre UV-transmitting

⁴<http://www.nso.edu/node/984>

⁵http://solis.nso.edu/0/info/solis_gallery.html [accessed on 27 January 2016]

fibre optic cable, which transmits light to a spectrograph in a temperature controlled room inside the telescope tower. To spatially homogenise the output light, small bends were introduced in the fibre to mix the modes transmitted by the fibre waveguide, which also helps to scramble the angular variations. The use of a fibre optic feed ensures the complete integration of the light in angular and spatial directions as required for Sun-as-a-star observations. For each wavelength band, ISS takes a sequence of four frames with a back-illuminated 512×1024 -pixel CCD camera. The data reduction includes a cloud detection algorithm (Pevtsov, Bertello, and Marble, 2014; Balasubramaniam and Pevtsov, 2011).

Another instrument to observe the Sun as a star is the Potsdam Echelle Polarimetric and Spectroscopic Instrument (PEPSI) for the Large Binocular Telescope in Southern Arizona (Strassmeier *et al.*, 2015). This high-resolution spectrograph has a spectral resolution of about $R = 310\,000$ and observes in the optical/red wavelength range from 390 – 1050 nm. It also includes the Solar-Disk-Integrated (SDI) telescope. Disc-integrated light from the Sun will get through two small Sun-as-a-star telescopes to a spectrograph via a fibre connection. PEPSI/SDI is designed to provide an external comparison source for high-resolution stellar spectroscopy and to monitor the Sun for measuring variations over the magnetic-activity cycle. In the future, comparing results from PEPSI/SDI and SOLIS/ISS and cross-calibrating the instruments will help determine instrumental effects potentially affecting the quality and accuracy of Sun-as-a-star spectra.

Chapter 5

Sun-as-a-Star Spectra

As one of the biggest telescopes for integrated sunlight spectra, SOLIS/ISS provides us high resolution integrated sunlight spectra, which we utilised in this work to find Sun-as-a-star chromospheric activity indices. Before using the data to develop new activity indices, we first had to become familiar with the data and make sure that we are handling it correctly. Therefore, we first plotted the spectra to get an overview of it in all wavelength bands. In addition, we reproduced the data of the Ca II K line and reconstructed the plots that are presented in Bertello *et al.* (2011), who used the same data for a shorter period, and show chromospheric activity indices. As in this chromospheric line one can see emission within absorption, there are three minima and two maxima visible around the line core, which are indicated as K1V, K2V, K3, K2R, and K3R from *left to right*, see Fig. 5.3, where *V* stands for *violet* and *R* for *red*. The plots in Bertello *et al.* (2011) show the variation of certain parameters in this line with time, also called time-series or light curves. More precisely, these parameters are the variation of the wavelength position and intensity of the line core K3, the $\lambda_{K2R} - \lambda_{K2V}$ and $\lambda_{K1R} - \lambda_{K1V}$ relations, the K2 to K3 asymmetry, the K2V to K3 ratio, and the 0.5 Å and 1 Å emission indices. The reconstruction of the plots provided us information about our understanding of the data, noise characteristics and potential error sources. The software that we developed for this purpose can then be used for future data from the Potsdam Echelle Polarimetric and Spectroscopic Instrument and the Solar Disk Integrated Telescope (PEPSI/SDI) data (Strassmeier *et al.*, 2015).

The high-resolution Sun-as-a-star spectra used in this work are based on level-2 data retrieved from the SOLIS/ISS FTP server.¹ The downloaded data consist of nine spectral bands (listed in Table 4.1), and the data presented in Fig. 5.1 were observed on 12 August 2012. The spectral bands cover important lines for solar physics (in the same plot from *left to right*): (a) the CN molecular band at $\lambda 388.4$ nm, (b, c) the strong chromospheric absorption lines Ca II K at $\lambda 393.4$ nm and Ca II H at $\lambda 396.8$ nm, (d) the C I spectral line at $\lambda 538.0$ nm, (e) the Mn I spectral line at $\lambda 539.4$ nm, (f) the Na D₁ spectral line at $\lambda 589.6$ nm, (g) the H α line at $\lambda 656.3$ nm, (h) the Ca II infrared line at $\lambda 854.2$ nm, and (k) the He I infrared line at $\lambda 1083.0$ nm, where the intensities in the panels are scaled differently for better display, and the continuum inten-

¹<ftp://solis.nso.edu/pubkeep>

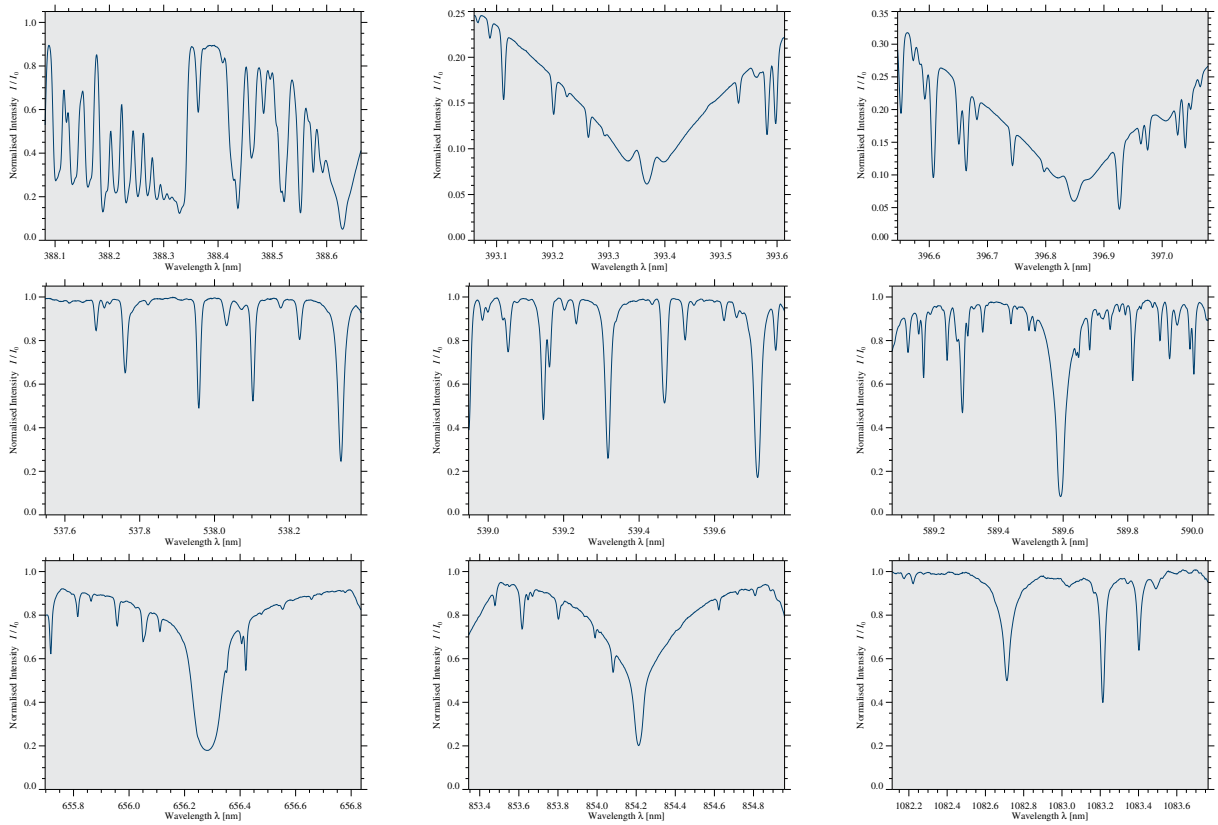


Figure 5.1: Spectral bands observed with SOLIS/ISS, which cover some of the most important lines for solar physics, from *left to right*: (a) the CN molecular band at $\lambda 388.4$ nm, (b, c) the strong chromospheric absorption lines Ca II K at $\lambda 393.4$ nm and Ca II H at $\lambda 396.8$ nm, (d) the C I spectral line at $\lambda 538.0$ nm, (e) the Mn I spectral line at $\lambda 539.4$ nm, (f) the Na D₁ spectral line at $\lambda 589.6$ nm, (g) the H α line at $\lambda 656.3$ nm, (h) the Ca II infrared line at $\lambda 854.2$ nm, and (k) the He I infrared line at $\lambda 1083.0$ nm. Note that the intensities in the panels are scaled differently for better display. The continuum intensity is normalised to unity.

sity is normalised to unity. Furthermore, the data are provided in Flexible Image Transport System (FITS, Wells, Greisen, and Harten, 1981; Hanisch *et al.*, 2001) format, with the FITS header containing information about the file name format (such as wavelength band, date, time), alongside the data format. The data is organised in three rows (wavelength in nanometers, normalised intensity, and estimated signal error), whereas only the intensity against the wavelength is plotted here. The plots show absorption lines that are formed in different heights of the solar atmosphere and are related to either a certain molecule or a chemical element. These are typical examples of integrated sunlight spectra observed on the same day in the different spectral bands and is meant to give us an overview of what the spectra look like. As the lines change with the presence of the magnetic field and the alteration of its strength, the Ca II H & K lines are major indicators for the magnetic field in the solar atmosphere and therewith the irradiation variability, (Pevtsov, Bertello, and Uitenbroek, 2013). Moreover, the Ca II K line is interesting for investigations of the morphology and evolution of the magnetic field, plages, and also for long-term observations, as there have been measurements of this line for over 100 years now (Bertello, Ulrich, and Boyden, 2010).

The left panel of the Fig. 5.2 shows the Ca II K line on 12 August 2012, with the marked line core as an example. The behaviour, meaning the variation of intensity and position, of this line

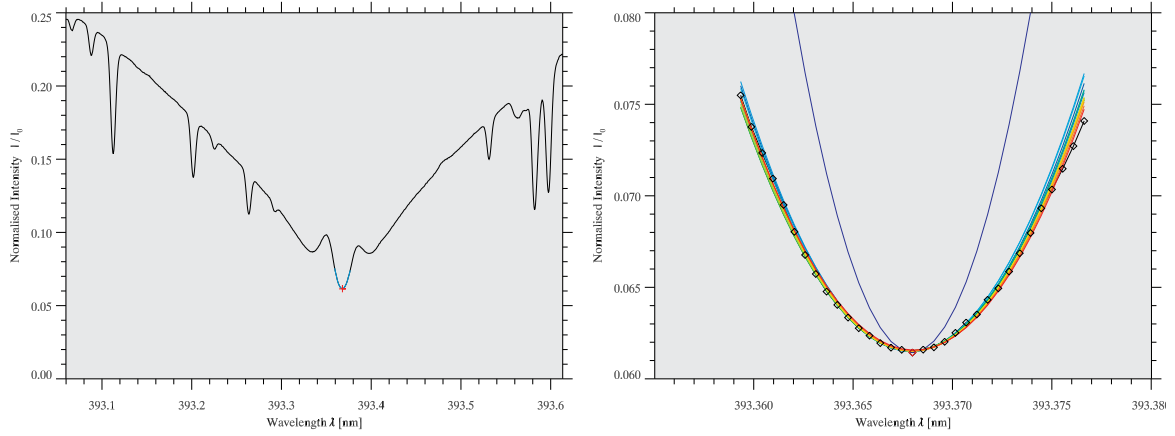


Figure 5.2: Ca II K line with light blue marked line core (*left*). This spectrum reveals the emission within the absorption of the Ca II K line (emission reversal). From left to right the minima or maxima are indicated with K1V, K2V, K3 (line core marked with red cross), K2R and K1R, respectively. The *right* plot shows the zoomed-in line core and illustrates the importance of the number of the data points used for the fitting obvious. Depending on the number, we get different curves when fitting the data points (represented by the diamond symbols) with a second-degree polynomial, whereas the red curves shows the fit with 33 data points and the violet curve the fit with only three points.

core over time is of high interest in this work. In order to investigate this behaviour, which is related to the chromospheric activity, we had to find the line core minimum first. To determine the actual minimum of the line core, the best polynomial fit needs to be found. Therefore, we determined the absolute minimum of the data points and fitted polynomials of second-degree into the 2 to 32 points around the data line core minimum, as indicated by the different colours. The right panel of Fig. 5.2 illustrates this procedure. Depending on the number of points that are included in the polynomial fit, the function changes and therewith the minimum of each graph changes slightly too. The exact differences in the minimum intensities can be seen in Table 5.1. It shows the pixel included to the polynomial fit (width), the according wavelengths, and the according intensity minimum of each graph. This facilitates the proper choice of the number of points that will be included in the second-degree polynomial fit, which is very important for the quality of the result.

In the next step, we want to find, in addition to the absolute minimum K3, the local maxima K2V & K2R (the maxima between the line core and the wings) and the local minima K1V & K1R (the minima between the emission peaks and the wings) that are closely related to the chromospheric phenomenon of emission reversal. We investigate their change with time as well, as they incorporate activity indices as well. Therefore, we initially smoothed the curve and then the indices of the local maxima K2V & K2R and minima K1V & K1R were obtained in four different ranges: (1) K1V: from the first spectral point to the approximate position of the inflection point between K1V and K2V, (2) K2V: from the inflection point to the rough intensity minimum K3, (3) K2R: from K3 to the position of the second inflection point between K1R and K2R, and (4) K1R: from the second inflection point to the last spectral point.

The selected broad ranges allow the determination of the minima and maxima, in case they vary strongly on a day-to-day-basis. After having determined the values for the minima and

Width	Wavelength λ [nm]	Intensity I/I_0
3	393.367981	0.061438
5	393.367950	0.061495
7	393.367920	0.061499
9	393.367920	0.061487
11	393.367889	0.061490
13	393.367889	0.061511
15	393.367889	0.061512
17	393.367889	0.061532
19	393.367920	0.061535
21	393.367920	0.061535
23	393.367950	0.061528
25	393.367950	0.061505
27	393.367981	0.061503
29	393.368011	0.061518
31	393.368042	0.061545
33	393.368073	0.061569

Table 5.1: The first column represents the pixel included in the second-degree polynomial fit, the second column the wavelengths of the Ca II K line core and the third column the intensity minimum.

maxima, we then proceeded to fit second-degree polynomials. The fitting procedure used the original spectral profiles because smoothing leads to a minimum with higher and a maximum with lower intensity. Only seven points were used to compute the second-degree polynomial (see the red ranges indicated in Fig. 5.3). In the same plot, the blue crosses mark initial estimates for the the minimum / maximum of the data and the green crosses mark the minimum / maximum obtained with the polynomial fit.

The line core K3 of the Ca II K line originates at temperatures of 7000 K, i.e., from the middle to the lower chromosphere, where its strength increases with increasing magnetic field strength, which is why Ca II K emissions are weaker in the quiet Sun than in the active Sun, for instance in regions of plages. The wings of the Ca II K, however, originate at even lower heights of the chromosphere than that of the temperature minimum (Skumanich *et al.*, 1984).

Replicated plots of the K3 lines that were originally presented in Bertello *et al.* (2011) constitute a good comparison to check, if our data processing techniques were correct, which is why we also kept the y ordinates as they are in the original plots. Note that, unlike in Bertello *et al.* (2011), our data reaches from 2007 to 2015 and thus extends the time series by four years (or 100%). In order to reconstruct all activity indices plots, ± 9 pixel around the minima or local maxima intensity constitute the base for the quadratic fit over these points. The choice of this range can be ascribed to Bertello *et al.* (2011) as well. The time-series plots for the K3 line core are depicted in Fig. 5.4, where the K3 wavelength position *left panel* and intensity *right panel* were plotted against time. Both plots show a greater variation of both, the wavelength position as well as the intensity as we reach solar maximum. The intensity time-series of K3 reveals

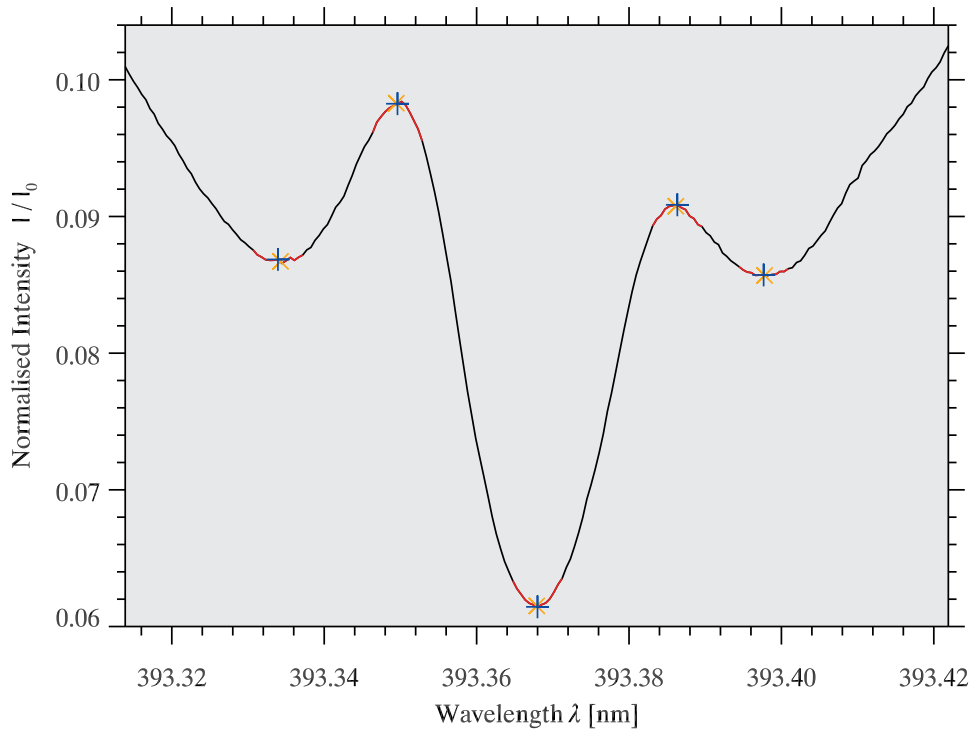


Figure 5.3: Ca II K line with marked absolute minimum K3, the local maxima K2V & K2R, and minima K1V & K1R in red. In this plot, the orange crosses mark the minimum or maximum of the fitted curve and the blue crosses mark the data minimum or maximum.

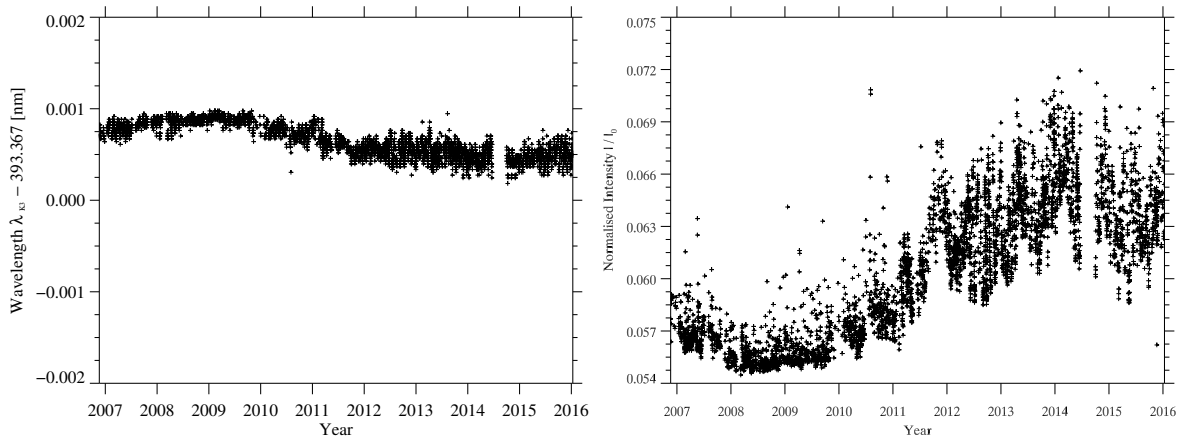


Figure 5.4: Ca II K line core (K3) wavelength position subtracted by the mean wavelength (*left*) and the intensity time series (*right*) as in Fig. 2 in Bertello *et al.* (2011), for the time from 2007 – 2016.

a close correlation to the solar cycle. We compared our K3 intensity wavelength time-series (*black*) to the one provided on the NSO website in December 2015 (*red*), which is illustrated in Fig. 5.5. We can see a small offset and trend for the overlapping time period, which result from the code Bertello *et al.* (2011) used to compute the parameter time-series. After providing the data and before computing the time-series Bertello *et al.* (2011) normalised the data “to preserve historical consistency” of archival KPVT observations (Bertello, priv. communication). This normalisation additionally leads to a smearing of about 1–2% of the effect of activity, which results in a trend. However, the new plots without this normalised data, which equal our plots, can now be found on the SOLIS website.² Thus, we can assume that our data processing was

²http://solis.nso.edu/iss/iss_timeseries.html

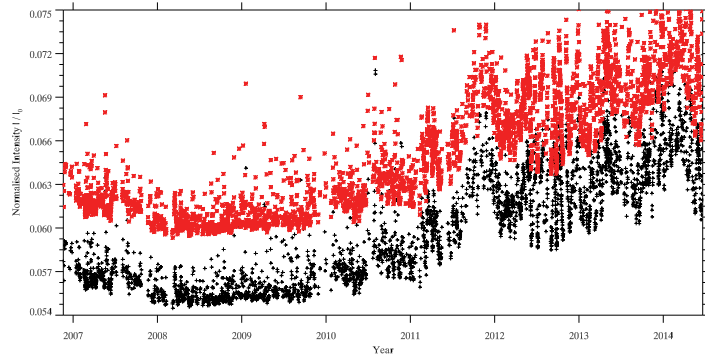


Figure 5.5: Ca II K3 intensity time series. Our plot (black) compared to the NSO plot from Bertello *et al.* (2011) (red) shows an offset and a trend. Note that the NSO plots have an additional normalisation.

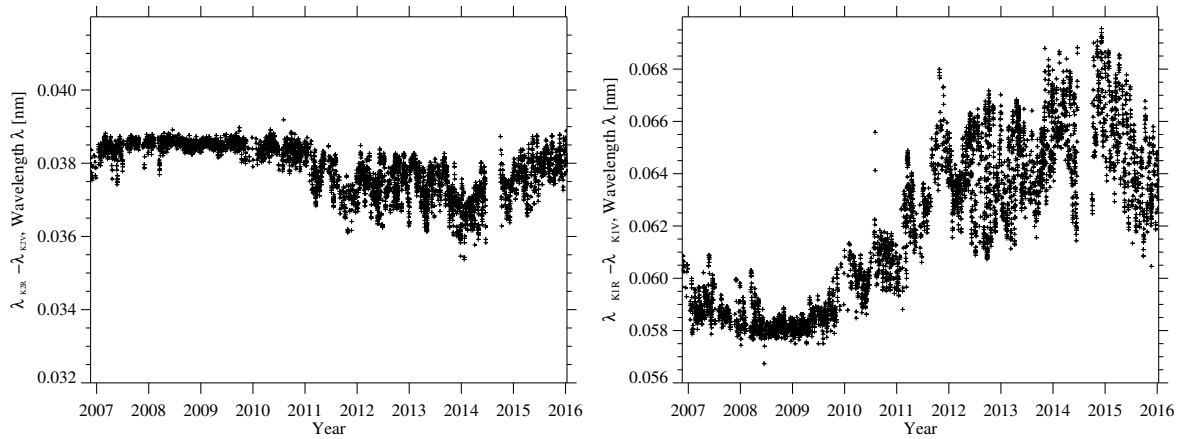


Figure 5.6: Ca II K $\lambda_{K2R} - \lambda_{K2V}$ (left) and $\lambda_{K1R} - \lambda_{K1V}$ (right) wavelength time-series, see Fig. 5 in Bertello *et al.* (2011), for the time from 2007 – 2016.

correct. The wavelength time-series of K1R–K1V shows the variation of the minima’s position in relation to each other, which varies to a higher degree than that of the maxima K2R–K2V, both shown in Fig. 5.6. However, the variation of the distance between the minima K1R and K1V, is correlated to the Sun’s activity: the wlarger the separation, the more active is the Sun. Considering this and regarding the plot, it can be assumed that the solar activity has increased since (roughly) 2010, as the separation has increased, which means that we have already reached the solar maximum and are now in the declining phase of solar cycle No. 24. Furthermore, the plot reveals that this spread varies much more during the maximum than the minimum, where it varies by 0.006 nm and 0.002 nm, respectively. What else is striking in the plot is the extended solar minimum, from 2007 until the end of 2009, and the two maxima in 2011. Comparing this to the SolarMonitor³ images in H α , one can see a clear correlation. When the distance of the two wavelength positions was large, the Sun was very active and shows various chromospheric features such on 20 October, 2011, where one can see many dark filaments and bright plages.

Other parameters that are derived from relations of the K3, K2R, and K2V are the K2-K3 asymmetry and the K2V/K3 ratio parameter depicted in Fig. 5.7. The K2-K3 asymmetry is calculated by dividing the according intensities

³<http://www.solarmonitor.org/index.php?date=20111020®ion=&indexnum=1>

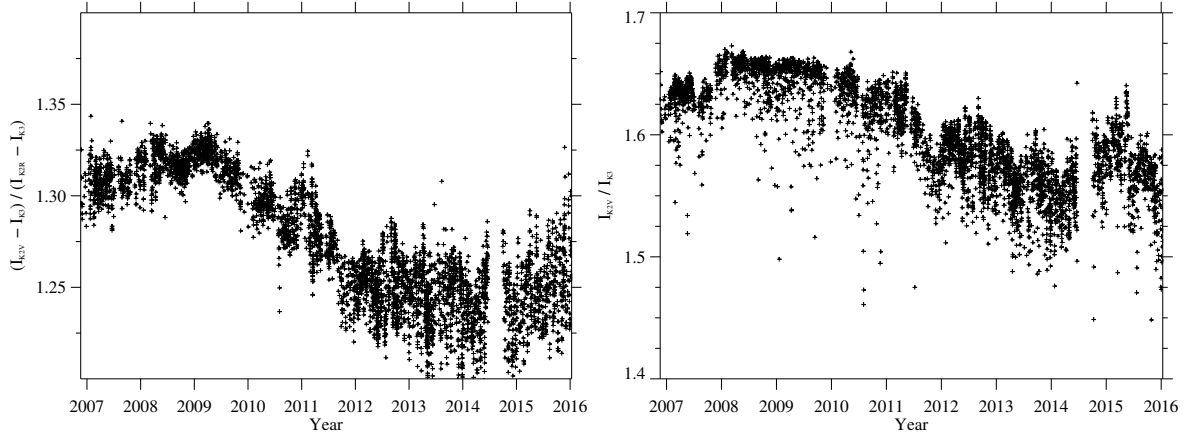


Figure 5.7: Ca II K K2 to K3 asymmetry and K2V to K3 ratio parameter time-series (see Fig. 6 in Bertello *et al.*, 2011), for the time from 2007 – 2016.

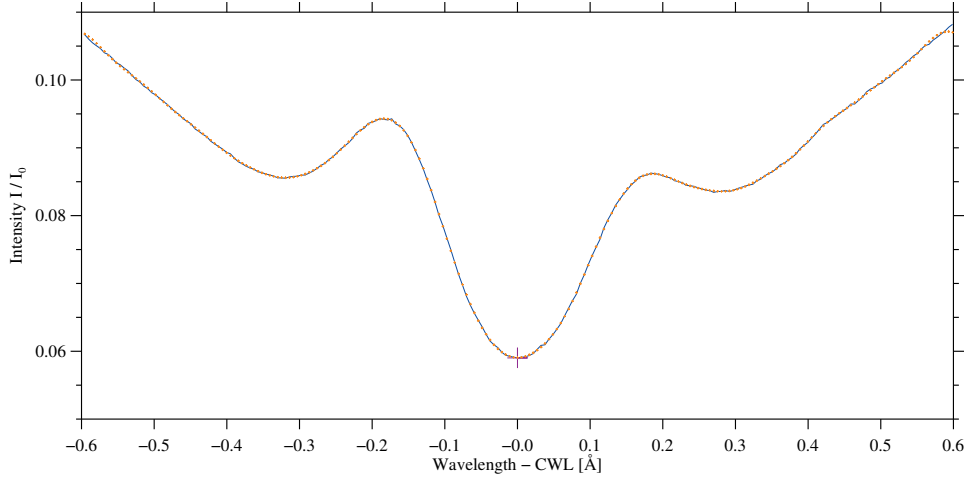


Figure 5.8: Ca II K reconstruction (crosses) of the observed spectrum (solid line) around the line core.

$$K2V/K3 = I_{K2V}/I_{K3}, \quad (5.1)$$

and the K2V/K3 ratio parameter is calculated with

$$K2 - K3 \text{ asymmetry} = (I_{K2V} - I_{K3}) / (I_{K2R} - I_{K3}). \quad (5.2)$$

In contrast to the other parameters, these two are anti-correlated to solar activity, and their lightcurves show a maximum at solar minimum and a minimum at solar maximum. Apart from those parameters, there are the 1 Å and 0.5 Å emission indices. They describe the area under the curve between -0.5 Å and $+0.5$ Å and also between -0.25 Å and $+0.25$ Å from the line core that changes with waxing and waning activity. To obtain these indices we adapted Eqns. 5.3 and 5.4, from Bertello *et al.* (2011). The first equation 5.3 serves for the reconstruction of the observed Ca II K line between -0.6 Å and $+0.6$ Å around the line core. As Fig. 5.8 shows, the

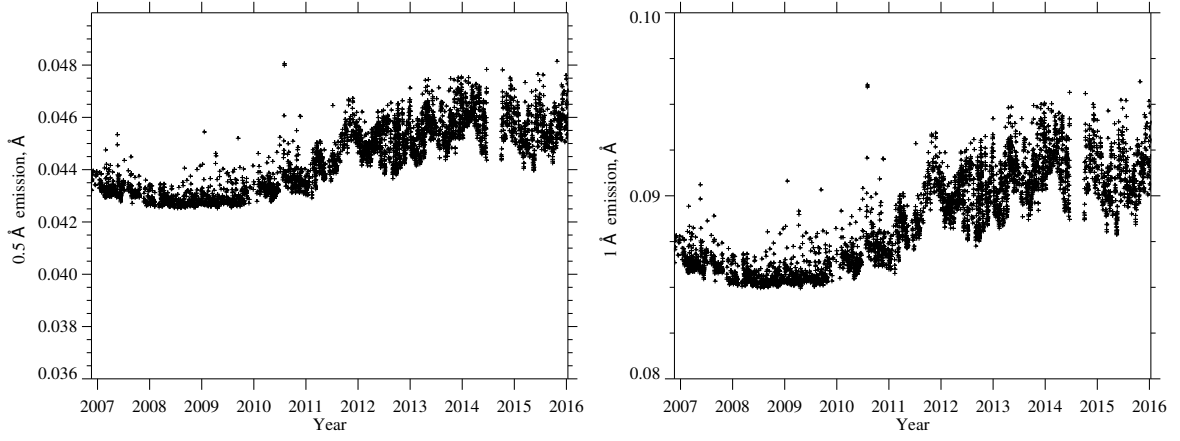


Figure 5.9: Ca II K 0.5 Å (*left*) and 1 Å emission index (*right*) time-series as depicted in Fig. 4 in Bertello *et al.* (2011) from 2007–2016.

model matches the observations around the line core very well.

$$I(x) = A_0 + 2 \sum_{i=1}^{NC} [A_i \cos(2\pi i x / N) + B_i \sin(2\pi i x / N)], \quad (5.3)$$

where $x = -N/2 + j$ and $j = 0 \dots N - 1$, N represents the number of spectral samples and NC the number of components needed for reconstructing the observed profile. The remaining coefficients A_i and B_i can be calculated by multiplying the given equation with either $\cos(2\pi i x / N)$ or $\sin(2\pi i x / N)$. Summing this over x and making use of the fact that sine and cosine are orthogonal, A_i and B_i can be determined. Having calculated all coefficients needed, the emission under the curve can then be calculated with following equation:

$$I(x) = A_0(x_2 - x_1) + 2 \sum_{i=1}^{NC} [A_i \cos(2\pi i(x_2 - x_1)/N) + B_i \sin(2\pi i(x_2 - x_1)/N)] - 2 \sum_{i=1}^{NC} [(B_i/i) \sin[2\pi i(x_2 + x_1)/N] \cos[2\pi i(x_2 + x_1)/N]] \quad (5.4)$$

Here, x_1 and x_2 are the limits, which means the points at -0.5 \AA and $+0.5 \text{ \AA}$ or -0.25 \AA and -0.25 \AA . The variation of this area or the emission index as a function of time can be seen in Fig 5.9 and reveals its close relation with the solar activity cycle.

Chapter 6

Activity Indices

Nowadays, it is commonly known that the solar activity changes, dominated by the 11-year solar cycle. For 70% of the Sun's lifetime, its magnetic activity is moderate, whereas in 15 – 20% and 10 – 15% it is in either a grand minimum or a grand maximum, respectively, affecting the solar-terrestrial relations as well (Usoskin, 2013). To investigate the Sun's activity and predict its variability, we can use such indices such as the sunspot number (SSN) and solar irradiance, shown in Chap. 2, that have a strong correlation to the activity. These two indices are very different from each other, as the sunspot number is a morphological index, revealed by the appearance of the Sun (sometimes visible with the naked eye), and the solar irradiance is a measured index, obtained by measurements of the intensity of the integrated light coming from the Sun. The change of solar activity can be found in each layer of the solar atmosphere and depends on the spectral range we observe. In the following we want to present the sunspot number, F10.7 cm radio flux index, Mg II index, and the TSI as representatives for the variation of the photosphere, higher chromosphere/lower corona, chromosphere, and integrated sunlight, respectively. At a later stage, we want to find a chromospheric Sun-as-a-star index for activity variability, derived from H α contrast profiles, and compare this to the already existing indices, presented in this section.

6.1 Sunspot Number

Through research and observations, the Solar Influences Data Analysis Center (SIDC) tries to increase our understanding of the Sun and its influence on the solar system. The World Data Center, which provides the Sunspot Index and Long-term Solar Observations (SILSO), is part of the SIDC. The data concerning the sunspot number are obtained from the World Data Center SILSO at the Royal Observatory of Belgium in Brussels,¹ where the SILSO website provides one of the longest dataset of sunspot numbers and therewith solar activity. Investigations of

¹<http://www.sidc.be/silso/datafiles>

long-term variations of solar activity can then help to study the solar cycle mechanism and the solar forcing on the Earth's climate.

Sunspots as such, are dark spots on the photosphere of the Sun. They appear to be dark, as their temperature (about 3800 K) is lower than that of the rest of the photosphere (Zeilik and Gregory, 1998, p. 215). We measure sunspots via the sunspot number, which indicates the number of dark spots that are visible on the surface of the Sun. However, this number changes with time, and a minimum of spots indicates the beginning of a new solar cycle (Zeilik and Gregory, 1998, p. 216).

The total number of sunspots is derived from the formula for the relative number of sunspots

$$R = k(N_s + 10 * N_g), \quad (6.1)$$

where N_s is the number of spots, N_g the number of groups counted over the entire solar disc, and k a scaling factor determined by Rudolph Wolf in the mid-19th century. The constant k is used to adjust the sunspot number for different observers, instruments, and sites. Note that for our data, $k = 0.6$ and hence the index R cannot take values between 0 (no spots) and 7 (single solitary spot, $R = 0.6 * 11$). Furthermore, there are currently no daily data provided before 1818 because there were barely daily observations, which is why we have only monthly and yearly means for all years before 1818.²

The daily total sunspot number files provided by SILSO contain data from 1 January 1818 to the last month elapsed. Our data was downloaded in May 2015, and hence span from 1 January 1818 to 30 April 2015. The format is in plain ASCII text with the following structure: column 1 is the Gregorian calendar date, column 2 is the date as a fraction of year, column 3 is the daily total sunspot number (a '?' symbol replaces the value when no data is available for that day), and column 4 represents the definitive/provisional marker. A blank indicates that the value is definitive and a '*' symbol indicates that the value is still provisional and is subject to a possible revision (usually the last three to six months of the entire data set).

The line itself gives information about the year [1–4 character position], month [5–6], day [7–8], decimal date [11–18], daily sunspot number [20–22], and the definite / provisional indicator [24].³ Figure 6.1 illustrates the variation of the sunspot number, and therewith the photospheric activity, from 1993–2015. Here, the blue curve is the lightcurve smoothed over 30 days and the yellow curve is the smoothed lightcurve over 200 days to reduce the diurnal variations.

Figure 6.2 shows the number of sunspots in each hemisphere, the northern (red) and the southern (blue) hemisphere. There is an asymmetry in the solar activity in the northern and southern hemisphere: as the solar cycle rises up to the maximum, the sunspots seem to appear

²<http://sidc.be/silso/infosntotdaily>

³<http://sidc.be/silso/infosntotdaily>

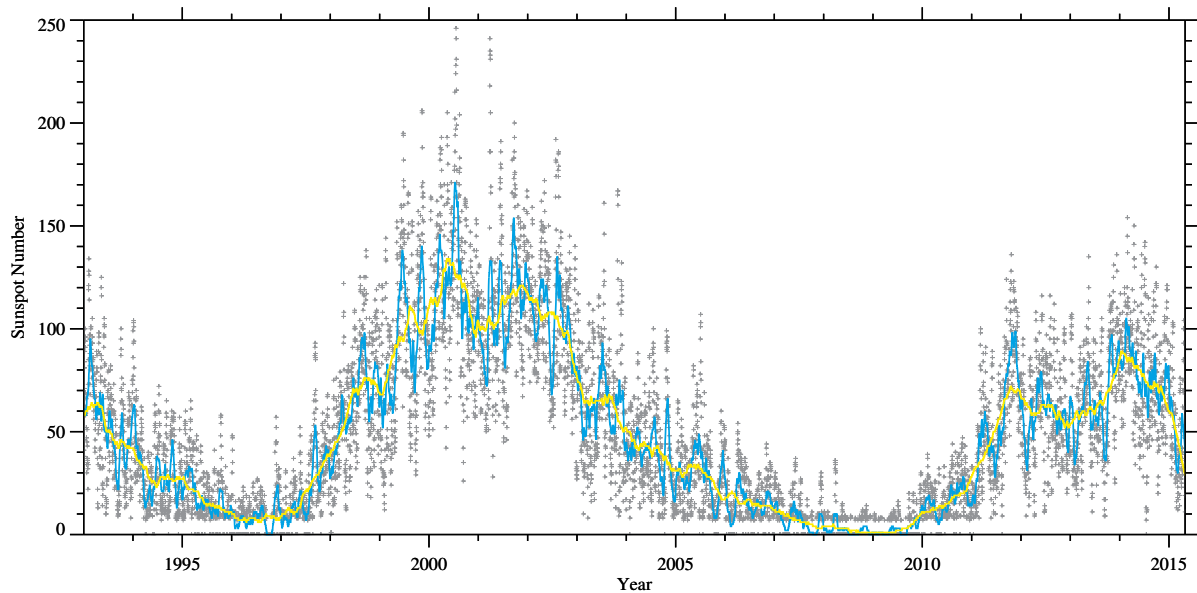


Figure 6.1: The variation of the SSN over two solar cycles or 22 years, smoothed over 30 days (blue) and over 200 days (yellow).

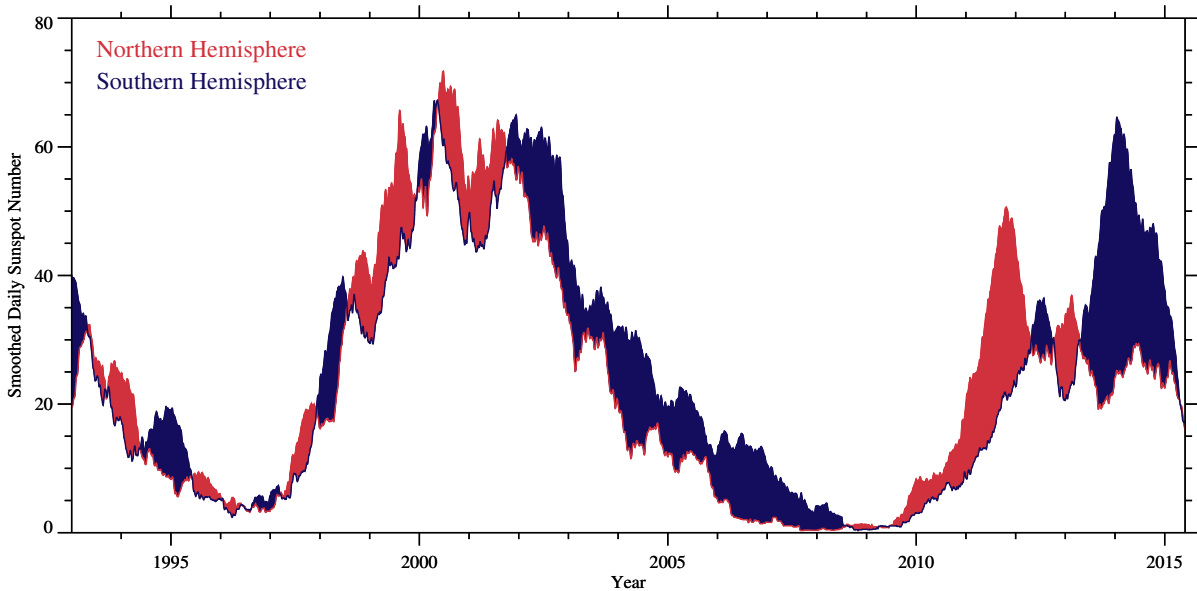


Figure 6.2: The variation of the SSN in the northern hemisphere (red) and the southern hemisphere (blue). Areas covered in red indicate the higher number of sunspots in the northern hemisphere at that time and areas covered in blue indicate the higher number of Sunspots in the southern hemisphere.

mainly in the northern hemisphere, whereas after the solar maximum they appear more in the southern solar hemisphere.

6.2 F10.7 cm Radio Flux

Another wavelength range that changes with the variation of the solar activity and has been observed for a long time (since 1947), is the solar radio flux density F10.7 cm at the wavelength

range of 10.7 cm, or 2800 MHz. This radio emission originates in the higher chromosphere and in the low corona of the solar atmosphere, either because of free-free emissions from hot coronal plasma or gyromagnetic emissions from active regions. Hence, it is a good quantitative measure for activity changes in the low corona or high chromosphere. The data is consistent and accurate, as measurements can be made from the ground in all weather conditions, and covers the time of six solar cycles, which makes it a valuable indicator. The F10.7 cm line is not directly related to the sunspot number, but their correlation (even though not linear and a bit more complex) shows that the sunspot number is a good indicator for the variation of the solar activity, not only in the photosphere, but also in the low corona or in general (Usoskin, 2013; Hathaway, 2010). The F10.7 cm index is given in solar flux units (sfu, with $1 \text{ sfu} = 10^{-22} \text{ W (m}^{-2} \text{ Hz)}^{-1}$)⁴ and can vary from below 50 sfu to above 300 sfu over the course of a solar cycle.⁵ This unit is used to express the flux density of radio energy from the Sun that is received at the Earth and is measured at the wavelength range of 10.7 cm, as this range correlates well with the Sun's output in the UV.

The data for this index can be accessed at the Space Physics data Facility of the Goddard Space Flight Center.⁶ Our data cover the period 1 January 1993 to 30 April 2015. The format of the Low Resolution OMNI (LRO) data set is the plain ASCII text, where the first column represents the year, the second the day-of-year (DOY), the third is the hour and the last column is the index. Note that the third column (hour) will always be 0, as the data contain the daily averaged index values. Furthermore, the NASA offers a 1963-to-current compilation of hourly-averaged, near-Earth solar wind magnetic field and plasma parameter data from several spacecraft in geocentric or Lagrange point (L1) orbits and provides other data that are connected to solar wind data. In addition to daily resolution, the data are available at hourly and 27-day resolutions. Figure 6.3 shows the variation of the value of the index with time for the given period.

Data points with much greater values than the signal would normally show are considered as noise or wrong signal, and were thus replaced by the median value. Therefore, five values were taken, two left and two right around the wrong signal point. The values of these five data points were ordered according to their size and the middle value was taken to replace the outlier. We replaced five data points of the F10.7 cm index, where the values were greater than 350 sfu. The plot clearly reveals the solar cycles and also shows that the activity in cycle 24 in the maximum is lower than in cycle 23. The blue line in this plot represents the light curve smoothed over 200 days and the yellow line the curve smoothed over 30 days.

⁴https://sizes.com/units/solar_flux_unit.htm

⁵<http://www.swpc.noaa.gov/phenomena/f107-cm-radio-emissions>

⁶<http://omniweb.gsfc.nasa.gov/ow.html>

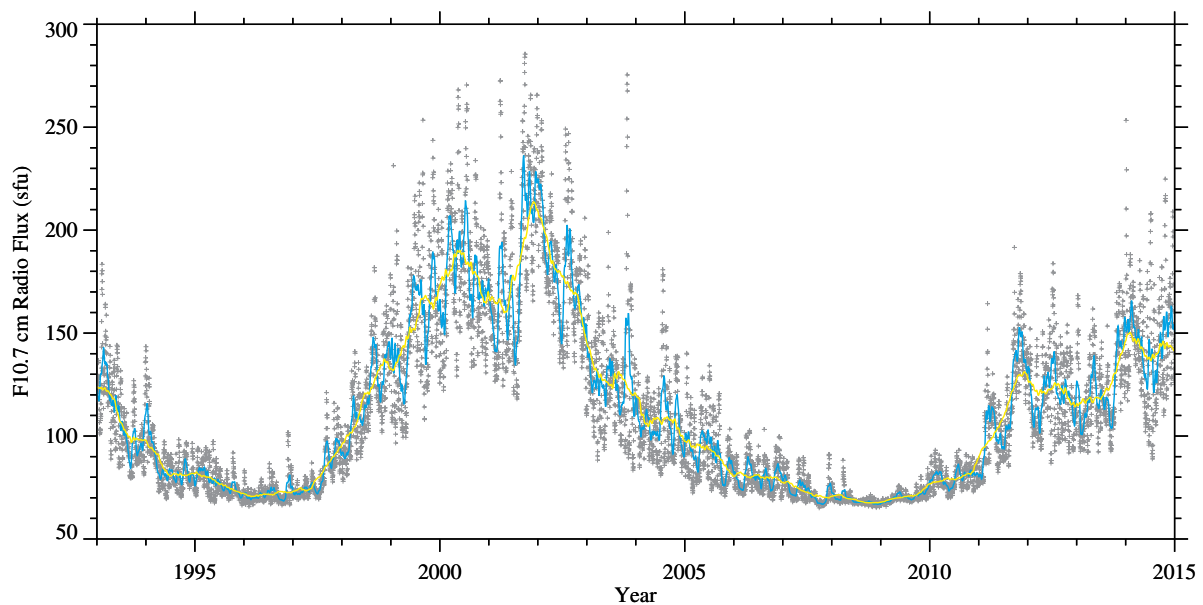


Figure 6.3: The time series of the solar coronal activity index F10.7 cm, from January 1993–April 2015. The blue line is the light curve smoothed over 200 days and the yellow curve smoothed over 30 days.

6.3 Mg II Index

An indicator of the chromospheric activity is the Mg II index, a core-to-wing ratio and observed from space (Thuillier *et al.*, 2012). The ratio is a measure of the amplitude of the chromospheric Mg II ion emission line core at 280 nm (UV) to the wings (solar continuum). The core originates in the higher chromosphere and the wings in the higher photosphere. This indicator is strongly correlated to the solar activity, especially to the irradiance variability in the UV and has, furthermore, the advantage of not being dependent on instrumental issues or variations. This is because ratios are much less sensitive to variations in instrument sensitivity, and as changes in the sensitivity are included in both the numerator and the denominator, any variations cancel out (Viereck and Puga, 1999). The phenomenon of an emission within an absorption line refers to the emission reversal of the chromosphere. As was already encountered in the Ca II K line 5.

Our Mg II index data are a composite created by the scientists of the University of Bremen and retrieved from their website.⁷ The data is a plain ASCII text and consists of five columns. The important columns are the first, listing the date, and the fourth, representing the Mg II Index, which has been observed since 1978. Figure 6.4 shows the variation of this index with time from 1993 until today, and illustrating its correlation with the solar cycle very well. Again, the blue line in this plot represents the light curve smoothed over 200 days and the yellow line the curve smoothed over 30 days.

⁷<http://www.iup.uni-bremen.de/gome/gomemgii.html>

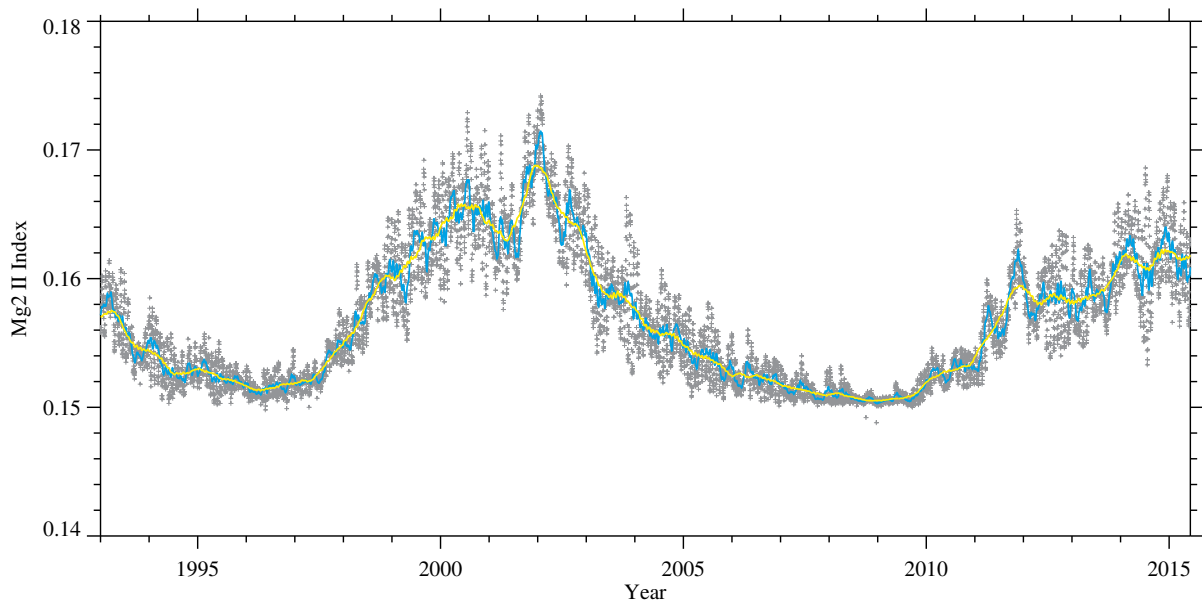


Figure 6.4: Mg II Index time series from 1993–2015. The blue line is the light curve smoothed over 200 days and the yellow curve smoothed over 30 days.

6.4 Total Solar Irradiance

The Total Solar Irradiance (TSI) is defined as the amount of radiant energy emitted by the Sun over all wavelengths crossing a square metre each second outside the Earth’s atmosphere (Hathaway, 2010, p. 14). The TSI is measured outside the Earth’s atmosphere because atmospheric absorption lead to inaccurate measurements, as it underlies uncertainties and fluctuations, although uncertainties are still present due to degradation of the instruments in space (Haigh, 2007, p. 24). The TSI is positively correlated with the solar activity and over the past 35 years it has shown a variation of 0.1% over the course of the solar cycle (Fröhlich, 2011). However, the TSI changes on all time scales due to the temporal evolution of magnetic phenomena on the solar surface such as sunspots, faculae, and chromospheric networks. Since it is the main energy input to Earth’s atmosphere, the TSI is used to develop climate models (Krivova, Solanki, and Schmutz, 2011).

The Solar Radiation and Climate Experiments (SORCE) total irradiance data, taken with the Total Irradiance Monitor (TIM),⁸ describe the spatially and spectrally integrated solar radiation reaching Earths atmosphere using an ambient temperature active cavity radiometer. TIM is one of five instruments of the SORCE spacecraft, which is mounted on a satellite observatory that orbits the Earth and accumulates solar data to continue, among others, the solar climate record that began 1978 in space. Moreover, TIM measures TSI at the top of the Earth’s atmosphere with an estimated absolute accuracy of 350 ppm (0.035%). Relative changes in solar irradiance are measured to less than 10 ppm/per year ($0.001\% \text{ yr}^{-1}$), allowing determination of possible long-term variations in the Suns output.

⁸<http://lasp.colorado.edu/home/sorce/data/>

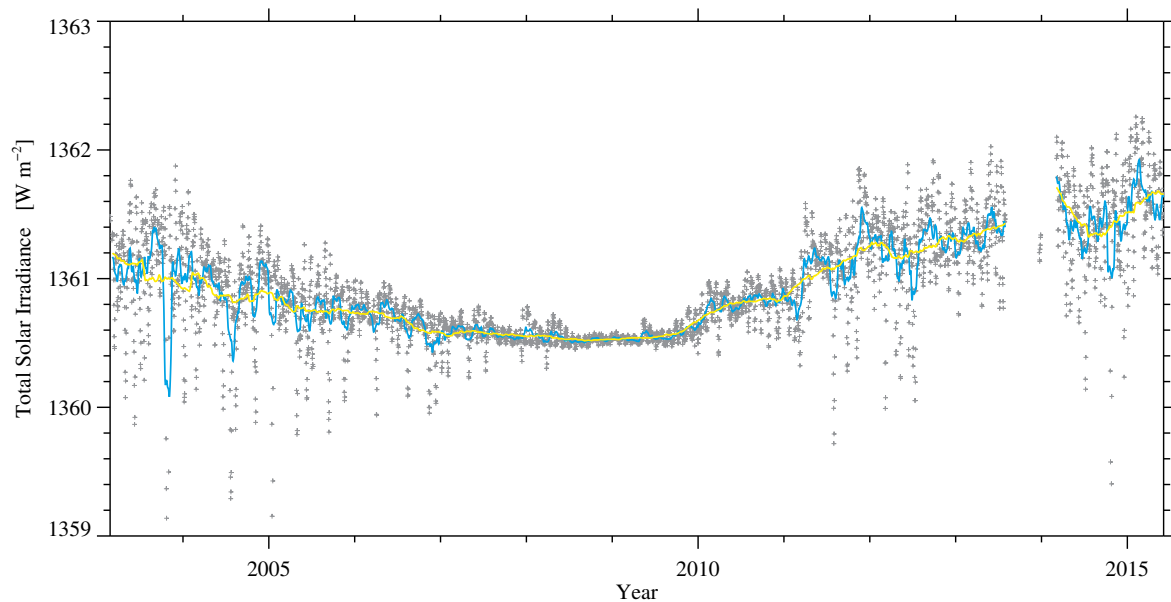


Figure 6.5: The variation of the total solar irradiance (TSI) from 2003–June 2015. The blue line is the light curve smoothed over 200 days and the yellow curve smoothed over 30 days. The gap from 2013–2014 is caused by a break of taking solar measurements. <http://lasp.colorado.edu/home/sorce/2014/08/14/daily-sorce-measurements-return/>

The SORCE spacecraft was launched in January 2003 to a 645-km high orbit at an inclination of 40° to the equator. We will be using data taken every day over twelve years, reported at a mean solar distance of 1 astronomical unit (AU) with units of Watt per square metre. Figure 6.5 is plotted with column 2 (Nominal Data Time, Julian Day Number) and column 5 (Total Solar Irradiance at 1 AU, W m^{-2}). We replaced 297 data points of the TSI by a mean value, where the total solar irradiance equals 0 and again, the blue line in this plot represents the light curve smoothed over 200 days and the yellow line the curve smoothed over 30 days. The TSI plot, however, is very different to the other indices because the variance is much smaller.

6.5 Linear Regressions and Correlation Coefficients of Scatterplots

The activity indices, shown in the previous section, all relate to different heights or atmospheric layers (photosphere, chromosphere, transition region, and corona) of the solar atmosphere. Furthermore, they can correspond to a particular band of electromagnetic radiation or some particle counts or relate to the occurrence of a certain feature (e.g., sunspots) on the Sun. What all the indices have in common, however, is that they are tied to the solar magnetic field. The motivation for this section is now to use some simple mathematical and graphical tools to quantify and illustrate the relationships among the solar activity indices – in preparation for the interpretation of the newly defined activity index based on H α contrast profiles (see Sect. 7.1). For that purpose, we use scatter plots, which reveal the behaviour of one index to a second index. Therefore, we might get a glimpse how solar activity is connected across spatial and temporal scales and how closely these ties are between different regimes/environments in the solar atmosphere.

The scatter plots that can be seen in Fig. 6.6 are crossed by a linear regression line. This line represents the fit of n data points to a straight line. In IDL this is realised with the *linfit* function that fits a straight line to the paired data x and y by using the linear model

$$y = a + bx. \quad (6.2)$$

As the IDL *linfit* function is based upon the *fit* and *gammq* routines taken from Numerical Recipes in C (Press *et al.*, 2002), a χ^2 -merit function underlies the *linfit* function

$$\chi^2(a, b) = \sum_{i=1}^N \left(\frac{y_i - abx_i}{\sigma_i} \right)^2. \quad (6.3)$$

It is basically a measure for the agreement between the data and the fitting model, or in other words, for how much the plotted curve deviates from the data points. It yields maximum likelihood parameter estimations of a and b , if the measurement errors are normally distributed and independent. Usually, the agreement is good, if the merit function is small. Hence, when a regression line is fitted, the parameters a and b are obtained by minimising a χ^2 -merit function (by determining the first derivation) as is shown in Eqns. 6.4 and 6.5. This is known as the best-fit and yields the best-fit parameters.⁹

$$0 = \frac{\partial \chi^2}{\partial a} = -2 \sum_{i=1}^N \frac{y_i - a - bx}{\sigma_i^2} \quad (6.4)$$

⁹<http://mathworld.wolfram.com/MeritFunction.html>

$$0 = \frac{\partial \chi^2}{\partial b} = -2 \sum_{i=1}^N \frac{x_i(y_i - a - bx)}{\sigma_i^2}. \quad (6.5)$$

This can be written as

$$S \equiv \sum_{i=1}^N \frac{1}{\sigma_i^2} \quad S_x \equiv \sum_{i=1}^N \frac{x_i}{\sigma_i^2} \quad S_y \equiv \sum_{i=1}^N \frac{y_i}{\sigma_i^2} \quad (6.6)$$

$$S_{xx} \equiv \sum_{i=1}^N \frac{x_i^2}{\sigma_i^2} \quad S_{xy} \equiv \sum_{i=1}^N \frac{x_i y_i}{\sigma_i^2}, \quad (6.7)$$

which leads to:

$$S_y = aS + bS_x \quad (6.8)$$

$$S_{xy} = aS_x + bS_{xx}. \quad (6.9)$$

Finally, the solution for the model parameters a and b are

$$\Delta = SS_{xx} - S_x^2 \quad (6.10)$$

$$a = \frac{S_{xx}S_y - S_xS_{xy}}{\Delta} \quad (6.11)$$

$$b = \frac{SS_{xy} - S_xS_y}{\Delta}. \quad (6.12)$$

The *linfit* function in IDL results in a two-element vector containing the linear model parameters a and b , which represent the (possibly) best fitting curve for a given set of data. However, there are uncertainties related to the estimates of a and b , which are due to the data having uncertainties, which are introduced to the calculation of the parameters, too. Taking into account the propagation of errors, the variance σ_f^2 can be expressed by:

$$\sigma_f^2 = \sum_{i=1}^N \sigma_i^2 \left(\frac{\delta f}{\delta y_i} \right)^2, \quad (6.13)$$

which leads to a variance in the estimates of the parameters a and b of

$$\sigma_a^2 = \frac{S_{xx}}{\Delta} \quad \text{and} \quad \sigma_b^2 = \frac{S}{\Delta}. \quad (6.14)$$

The covariance and the correlation coefficient of a and b indicate, if they behave similarly and have the same sign, respectively. The correlation coefficient is the normalised version of the covariance, and therefore shows values between -1 and $+1$.

The correlation coefficient r describes how closely data fall along a straight line in a scatter plot and is a measure of the degree of the linear dependence of two variables. Thereby, r can take values between -1 and $+1$. The closer r is to one, the more it can be described by a linear equation. If r is $+1$ the correlation is called a “complete positive relation”, with a positive slope

and increasing values of both variables. Whereas, if r is -1 it is termed a “complete negative relation”, with a negative slope and an increase of one variable when the other is decreasing. If r is close to zero, there is only a very weak or no linear relationship at all between the data points, and the variables are uncorrelated (Press *et al.*, 2002, p. 636). The correlation coefficient r is described as

$$r = \frac{\sum_i (x_i - \bar{x})(y_i - \bar{y})}{\sqrt{\sum_i (x_i - \bar{x})^2} \sqrt{\sum_i (y_i - \bar{y})^2}}. \quad (6.15)$$

In IDL this correlation coefficient is computed using the function `correlate(x, y)`. Technically speaking, the numerator of this equation is the covariance of the two variables x and y and the denominator is the product of each of the standard deviations. The covariance describes to what extent the variables x and y change together. It is positive when the variables show similar behaviour and negative when they show opposite behaviour.¹⁰

However, if r is close to zero, it does not mean that there is no correlation at all, but only that there is no linear correlation. But if the coefficient is indeed positive or negative it is still not for sure that the variables are linearly correlated or that there is a linear dependence. There are several conditions that have to be fulfilled. One of them is that the difference of the coefficient from zero has to be significant. This can be proven by tests like the Student t -test but it is still difficult to say when a correlation coefficient is significant and if one coefficient is more significant than the another. The difficulty in interpreting the significance of this linear correlation coefficient led to the approach of nonparametric or rank correlation (Press *et al.*, 2002, p. 639).

An example of a rank correlation is the Spearman correlation coefficient ρ that is implemented in IDL by the `r_correlate` function of the measurements x and y . The difference of a rank correlation is that it is nonparametric, and the coefficient does not depend on the normal distribution of the parameters, hence is more robust. Here, the value of the x_i and y_i are replaced by the value of their rank (1, 2, 3, ..., n) among the other x_i or y_i , respectively. The ranked values can now be described by the known uniform distribution of integers from 1 to n with the sum for natural numbers being $n(n + 1)/2$. It is more resistant to outliers, like the median is more robust than the mean, but replacing the actual values with their rank is connected to loss of information, too. However, if a correlation can be detected nonparametrically, then there definitely is a correlation.

After replacing the values, the rank-order correlation coefficient is determined by taking the linear correlation coefficient of the ranks into account.

¹⁰www.realstatistics.com/correlation/basicconcepts/correlation/

$$\rho = \frac{\sum_i (R_i - \bar{R})(S_i - \bar{S})}{\sqrt{\sum_i (R_i - \bar{R})^2} \sqrt{\sum_i (S_i - \bar{S})^2}}. \quad (6.16)$$

,where R_i is the rank of x_i and S_i the rank of y_i . Additionally, the significance of a nonzero value of ρ can be tested with

$$t = r_s \sqrt{\frac{N-2}{1-\rho^2}}. \quad (6.17)$$

Therefore, Spearman's ρ is mainly a special case of Pearson's r , where the data is ranked according to their value beforehand.

In order to illustrate if and how two indices correlate with each other, one index is plotted against another. This can only be achieved, if the data sets have the same date format and if the days match for which there exists an entry. Therefore, the given dates were converted into the date format `yyyymmdd`. The index values with the according date are saved in native IDL file format (`*.sav`) of the same name.

If two indices correlate with each other, it means that they behave similarly. If one index changes the other will change. In addition, it means that if they correlate, the corresponding atmospheric layers correlate and we can draw conclusions about the layers' connection. The sunspot number is representative for the variation of the photosphere, F10.7 cm radio flux index for the higher chromosphere/lower corona, Mg II index for the chromosphere, and the TSI is representative for the variation of the integrated sunlight. The scatter plots presented in Fig. 6.6 all exhibit a positive correlation of the activity indices with each other. Comparing this to the time-series shown earlier in this chapter, we can see a similar behaviour with time. The linear correlation coefficient and the rank order correlation coefficient differ when the data have many outliers, because the rank order correlation coefficient is more resistant to it, and hence yields a higher correlation coefficient. For data with fewer outliers the difference is negligible. An overall good correlation can be found in the scatter plot of the sunspot number and the F10.7 cm radio flux index. There, the correlation is best at low sunspot numbers and a low F10.7 cm radio flux index, which means when the Sun is less active or at solar minimum. At higher values for each, one can see a stronger scattering of the data points and more outliers. This is because towards solar maximum the activity and measurements of the indices vary to a higher degree, also revealed in the time-series plots (6). The gap in the scatter plots containing sunspot number data is due to the definition of the relative sunspot number, as this allows a sunspot number only higher than eleven, see Eqn. 6.1. What is furthermore conspicuous is that the correlation of the indices with the TSI is very poor. This could be due to the difficulty of calibrating TSI data. Later in this work, we want to examine how well our $H\alpha$ index correlates with one of these indices.

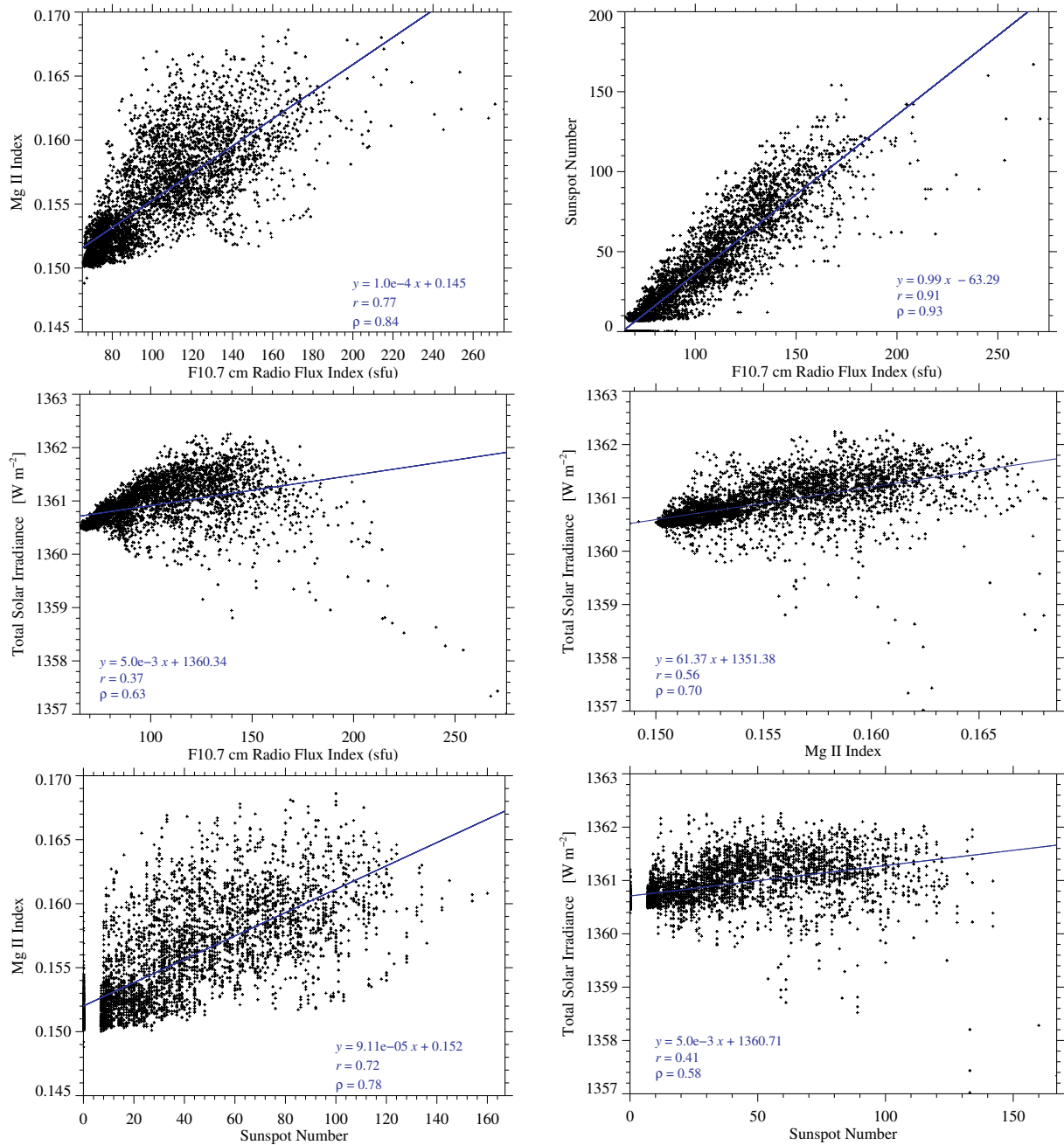


Figure 6.6: Scatter plots of (a) the F10.7 cm index against the Mg II index, (b) the F10.7 cm index against the sunspot number, (c) the F10.7 cm index against the TSI, (d) the Mg II index against the TSI, (e) the sunspot number against the Mg II index, (f) the sunspot number against the TSI.

Chapter 7

Activity Index from H α

7.1 Cloud Model

In 1964 Beckers developed an approach to solve the radiation transfer equation and therewith retrieving line formation parameters for an observed structure (Beckers, 1964). This is today known as the cloud model (CM). It is a common inversion technique, or a procedure to obtain parameters for a model from observations. The model describes how the structures that lie above the photosphere influence the radiative transfer of the incident light from the photosphere. These structures can be considered as clouds similar to those on Earth that absorb, emit, and scatter the incident light. This process can be described by (Tziotziou, 2007)

$$I(\lambda) = I_0(\lambda)e^{-\tau(\lambda)} + \int_0^{\tau(\lambda)} S_t e^{-t(\lambda)} dt, \quad (7.1)$$

where the first term on the right constitutes the absorption and the second term the emission by the cloud. The function $I(\lambda)$ is the observed spectral intensity, $I_0(\lambda)$ is the profile of the incident radiation (emitted by the background) that serves as a reference profile, $\tau(\lambda)$ is the optical thickness, and S is the source function. The model was motivated by Beckers aim to find the velocity of a filament channel not by looking at the displacement of the line core but by finding the wavelength, where one can see a maximum contrast (Beckers, 1964, p. 30).

Following Eqn. 7.1, the radiative transfer through this material depends on its optical thickness, which is one of four parameters that can be extracted from the model (Tziotziou, 2007). Others are the Doppler shift, the Doppler width and the source function. However, the cloud model can only be applied, if the structure, which we want to investigate, is fully separated from the underlying chromosphere, thus it requires a background profile in H α . This background profile $I_0(\lambda)$ represents the irradiation from the parallel, underlying structure (hence the cloud receives uniform radiation from below) or an average quiet-Sun spectral profile. Its choice plays an important role for the resulting CM parameters (Bostanci and Al Erdoğan,

2010). Moreover, the background intensity has to be the same below and around the cloud, and therefore can be extrapolated from a neighbouring region. In addition, it is assumed that the source function, radial velocity, Doppler width, and the absorption coefficient are constant along the LOS (Tziotziou, 2007). Considering these assumptions, the radiative transfer equation can be simplified to

$$I(\lambda) = I_0(\lambda)e^{-\tau(\lambda)} + S(1 - e^{-\tau(\lambda)}) \quad (7.2)$$

and can be written as

$$C(\lambda) = \frac{I(\lambda) - I_0(\lambda)}{I_0(\lambda)} \quad (7.3)$$

or

$$C(\lambda) = \left[\frac{S}{I_0(\lambda)} - 1 \right] \left(1 - \exp[-\tau(\lambda)] \right) \quad \text{with} \quad (7.4)$$

$$\tau(\lambda) = \tau_0 \exp \left[- \left(\frac{\lambda - \lambda_c}{\Delta\lambda_D} \right)^2 \right], \quad (7.5)$$

where $C(\lambda)$ is defined as the contrast profile, which shall, in the following, help us to investigate characteristics of the strong chromospheric absorption lines. The LOS velocity v_c of the cloud can be derived, once λ_c is known, according to

$$v_c = c \frac{\lambda_c - \lambda_0}{\lambda_0}, \quad (7.6)$$

where λ_0 is the central wavelength and c the speed of light. Since Beckers invented the CM there have been several techniques suggested to improve the output of the physical parameters, (see Tziotziou, 2007). However, in this work, we just use the classical CM.

For the contrast profile we need to determine a background profile, which choice is essential to the outcome of the parameters that can be derived from it (Tziotziou, 2007). We assume, like Beckers, that the background profile of the incident light on the structure is the same as the reference intensity profile. It is obtained from the average of spectral profiles over the reference regions, which is based on the assumption that the space between the reference region and the structure is transparent to light (Chae, 2014). For us, the reference region is the whole solar disc (Fig. 7.4) and the reference profile is the mean of 14 days of quiet-Sun profiles in H α (Fig. 7.5).

7.2 H α Centre-to-Limb Variation

The model assumes that the cloud receives uniform radiation from below, which is the background profile $I_0(\lambda)$, visible in H α . However, David (1961) showed that the continuum intensity and spectral shape of the H α line change from the solar disc centre to the limb. This

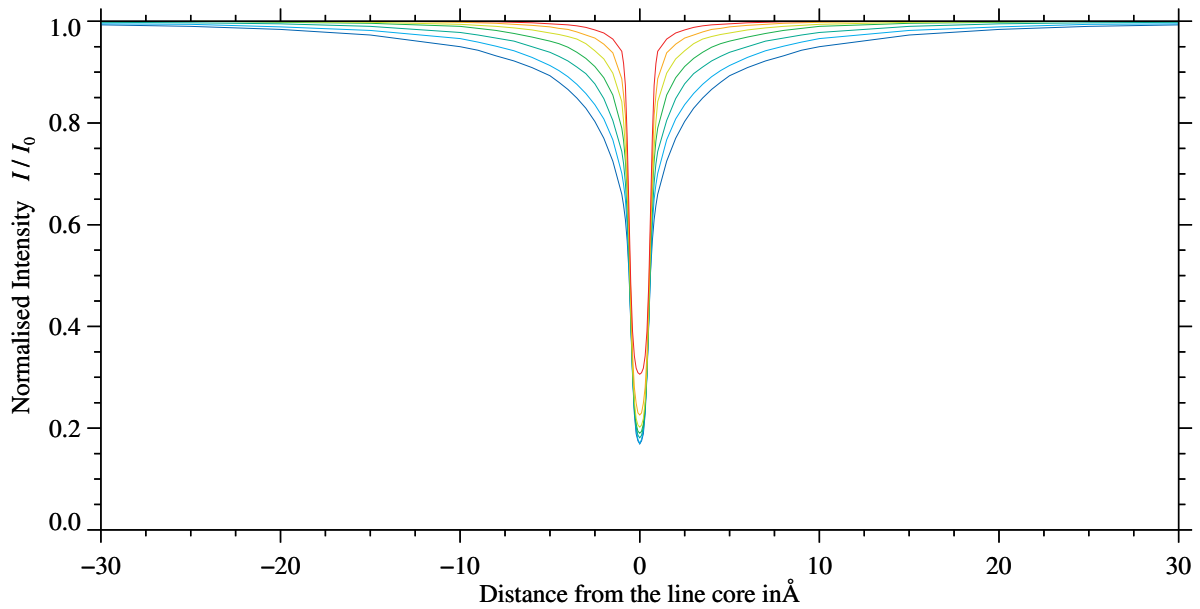


Figure 7.1: Centre-to-limb-variation of the strong chromospheric absorption line $H\alpha$. The spectral intensity is plotted as a function of distance from the line centre with data from [David \(1961\)](#). The spectra were normalised to local continuum and the rainbow colour code indicates the distance from solar disc-centre with red referring to the cosine of the heliocentric angle of $\mu = \cos \theta = 0.141$ and violet ($\mu = 1$) corresponds to the $H\alpha$ profile at disc-centre.

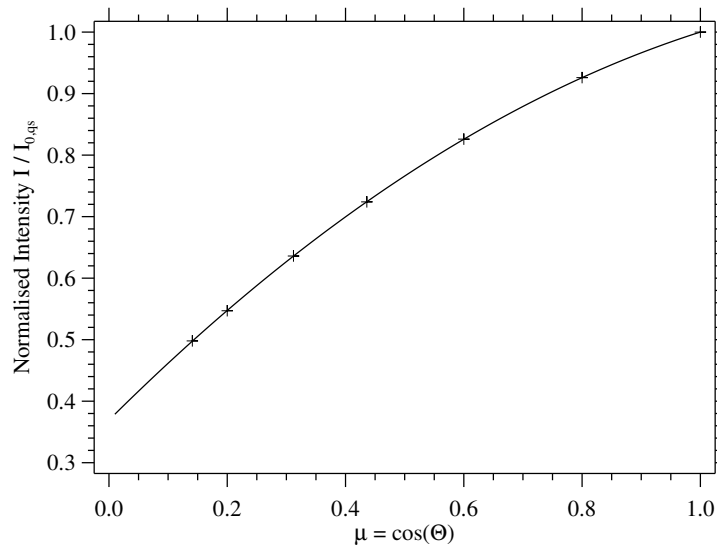


Figure 7.2: Centre-to-limb variation of the $H\alpha$ continuum intensity, where μ refers to the cosine of the heliocentric angle θ . The seven crosses mark the positions on the disc, where the profiles plotted in [Fig. 7.1](#) were taken and the solid line is a second-degree polynomial fit to the data points concerning the full range from the solar limb to disc-centre.

variation depends on the heliocentric angle, which is illustrated in [Fig. 7.1](#) and plotted with data excerpted from [David \(1961\)](#). The local continuum is normalised to unity and the x -axis shows the distance from the line centre. The violet line represents the $H\alpha$ profile at the centre and the red line at the limb. The intensity of the line at the centre is lower than that at the limb. Therefore, the photons coming from disc-centre are absorbed more strongly because the the line core is deeper. In addition, at disc-centre the wings are more pronounced, which implies that the atmosphere is more opaque for photons in these spectral regions as well. However, at the limb predominantly photons with a wavelength very close to the line core are absorbed.

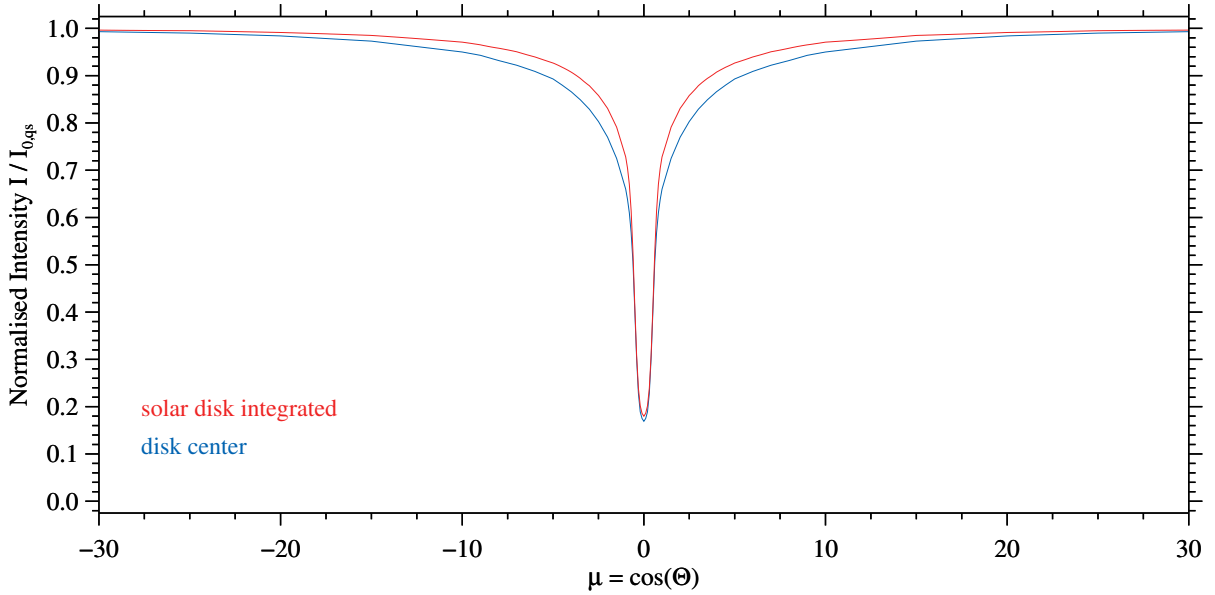


Figure 7.3: Disc-integrated $H\alpha$ absorption line (*red*) and $H\alpha$ spectrum observed in the disc centre (*blue*) based on spectral intensity data presented in David (1961).

In Fig. 7.1, the spectral intensities were normalised to the local continuum I_0 , and plotted as a function of the distance from solar disc centre. The centre-to-limb variation of the continuum radiation is presented in Fig. 7.2 based on the data provided by (David, 1961). Here, the spectra were normalised to the continuum intensity at disc centre $I_{0,qs} = I_0(\mu = 1)$. The spectral data of David (1961) were given for only seven positions on the solar disc. Therefore, a 2nd order polynomial was fitted to these data points covering all disk positions from the solar limb to disc centre.

As already seen Fig. 7.1, the shape of the strong chromospheric absorption line $H\alpha$ depends on the disc position, as does the continuum intensity, which was demonstrated in Fig. 7.2. This leads to the questions: what is the spectral shape of a disc-integrated $H\alpha$ profile? To answer this questions, we interpolated the $H\alpha$ spectra on an equidistant grid of 1 \AA in wavelength in the range from $\pm 30 \text{ \AA}$ and of 0.01 in μ in the interval from zero to unity. The two-dimensional interpolation used Delaunay triangulation (Lee and Schachter, 1980). Finally, the spectra for each disc position were averaged according their frequency of occurrence on the solar disc, and the result was normalised to the continuum intensity at disc centre $I_{0,qs}$. The results depicted in Fig. 7.3 show a much narrower $H\alpha$ profile with less pronounced line wings as compared to the profile at disc-centre. This brief numerical exercise clearly demonstrates the necessity to find an appropriate background profile, if a more advanced interpretation of $H\alpha$ Sun-as-a-star spectra, for example in the context of CM inversions, is desired.

7.3 Contrast Profiles

As we have just learnt, the spectrum in $H\alpha$ integrated over the solar disc shows a different shape than does the resolved spectrum for the same line. However, the former will allow us to compare the solar spectra with stellar spectra and make conclusion about other stars. To now apply the CM, we need a reference spectrum which is given by the quiet-Sun spectrum in $H\alpha$. Georgi Kokotanekov found, during his summer project at the AIP, 14 days between January 2007 and May 2010 where the Sun was very quiet or inactive, and by implication, showed neither flares, nor bright plage areas, nor active regions in the $H\alpha$ images. An example of what the quiet-Sun in $H\alpha$ ¹ and the corresponding magnetogram² looked like is shown in Fig. 7.4. The magnetogram represents the strength of the magnetic field on the Sun that varies spatially. This strength can be inferred from the investigation of the Zeeman splitting of spectral lines. The magnetogram reveals a low magnetic field strength when the Sun is quiet. The quiet-Sun seen in the continuum³ and extreme ultraviolet (EUV)⁴ are depicted in the bottom part of the figure. All images show that when we have a quiet Sun, features related to strong magnetic fields are not present, thus the magnetic field strength is very low, and the surface has a uniform appearance over a broad wavelength range.

The spectrum of the quiet-Sun in $H\alpha$ is shown in Fig. 7.5. It comprises Sun-as-a-star spectra of 14 days when the Sun was quiet and in the minimum phase of the solar cycle. The absorption lines beyond the line core are telluric lines and need to be removed at a later stage. The average spectrum will serve as a reference background profile for the contrast profiles, which constitute the basis for applying the cloud model to solar disc-integrated spectrum.

The procedure for calculating a contrast profile of our observed and fitted spectra starts with a fit of the $H\alpha$ average quiet-Sun spectrum with the IDL function `mpcurvefit`, including a triple Voigt function. Figure 7.6, exhibits in the *left* panel the whole spectral range and in the *right* panel the zoomed-in line core of the averaged $H\alpha$ quiet-Sun spectrum. A triple Voigt function is needed because the Sun as a whole rotates, whereby one edge is moving away and the other one is moving towards us. This leads to a broadened line core, which cannot be fitted with a single Voigt function. For the fit, one of the three Voigt functions is centered at the line core and the other two are equidistantly spaced profiles. The *black* curve represents the observed average quiet-Sun profile, and the *red* curve shows our attempt to fit the curve and erase telluric absorption features in the wings. The vertical line marks the line core centered at 656.281 nm. The plot also shows how well our fit matches the observations. As a next step, we computed the contrast profiles, using Eqn. 7.1, from the observed spectra (the observed $H\alpha$ spectrum and the observed quiet-Sun average spectrum) and the fitted spectra (fitted $H\alpha$ spectrum and fitted quiet-Sun average spectrum) and plotted this as a collage depicted in Fig. 7.7. The plots

¹www.solarmonitor.org/full_disk.php?date=20090204&type=bbso_half&indexnum=1

²www.solarmonitor.org/full_disk.php?date=20090204&type=smdi_maglc&indexnum=1

³<http://sohowww.nascom.nasa.gov>

⁴<http://sohowww.nascom.nasa.gov>

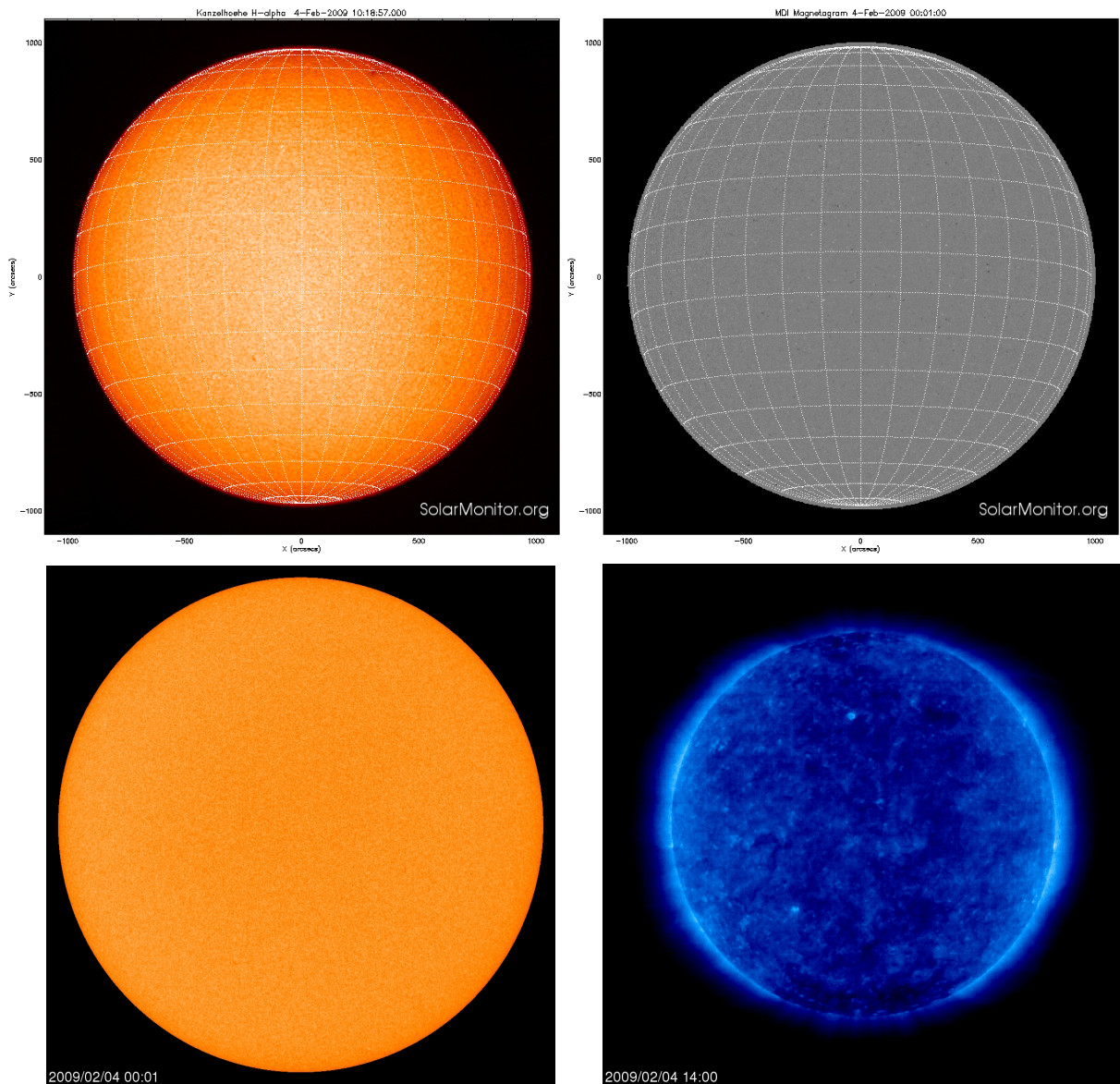


Figure 7.4: Quiet-Sun images in $H\alpha$ (*upper left*), magnetogram (*upper right*), continuum image (*bottom left*), and EUV image (*bottom right*) on 4 February 2009.

illustrate the intensity of the contrast profile with time, where the spectrum is turned by 90° clockwise and one spectrum added to the next, which results in a wavelength-time collage. The data gap in late 2014 was caused by relocating SOLIS/ISS from KPNO to NSO headquarters in Tucson, Arizona. Black indicates low contrast and white indicates high contrast. The *top* panel is a collage of the observed contrast profiles, where the telluric lines are still distinct and the *bottom* panel contains the fitted contrast profile collage, scaled in the range from ± 0.1 and -0.05 to 0.1 of intensity, respectively. The two horizontal red lines mark the spectral region with enhanced contrast in $H\alpha$, which is around the line core. As we can see, the contrast in that region increases with time and has its maximum at the end of our data, which is January 2016. The plot starts in August 2007, where we have a solar minimum and we are in solar maximum of cycle 24 in 2014 (compare Fig. 6.1). The strong rise starting in mid-2015 is not correlated with the decline of solar activity at that time. These latest data also deviate from measurements just after relocating SOLIS/ISS from a mountain site to less favourable site in an metropolitan

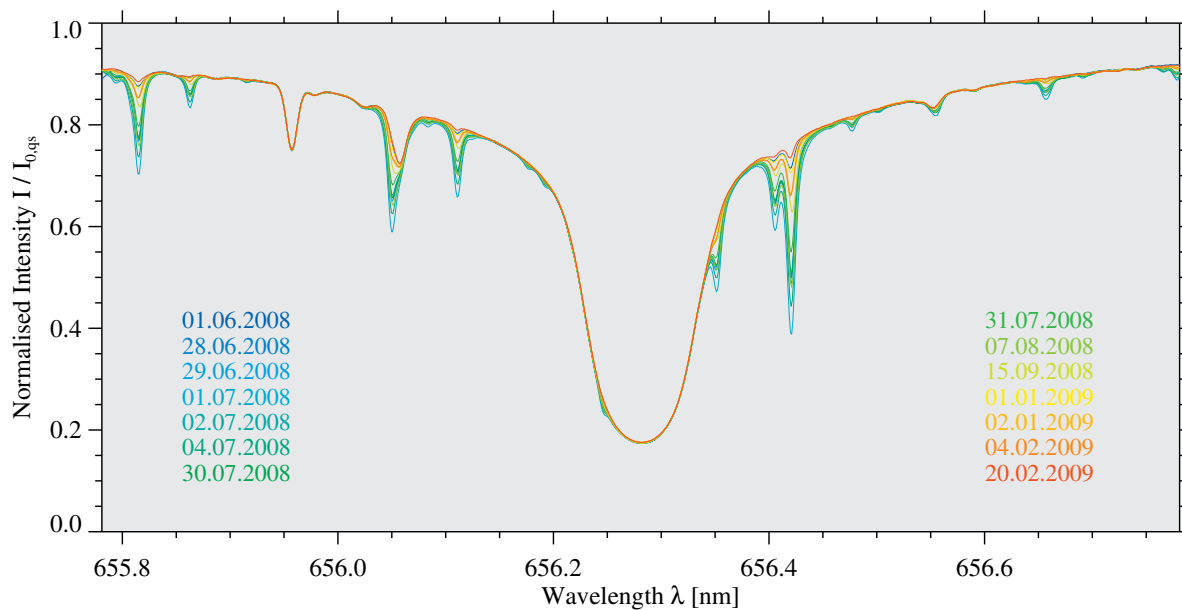


Figure 7.5: Disc-integrated H α quiet-Sun profiles (plotted with ISS data) on 14 different days, where neither strong magnetic fields nor any major H α absorption features were present on the solar disc. Spectra and corresponding observing dates are colour-coded.

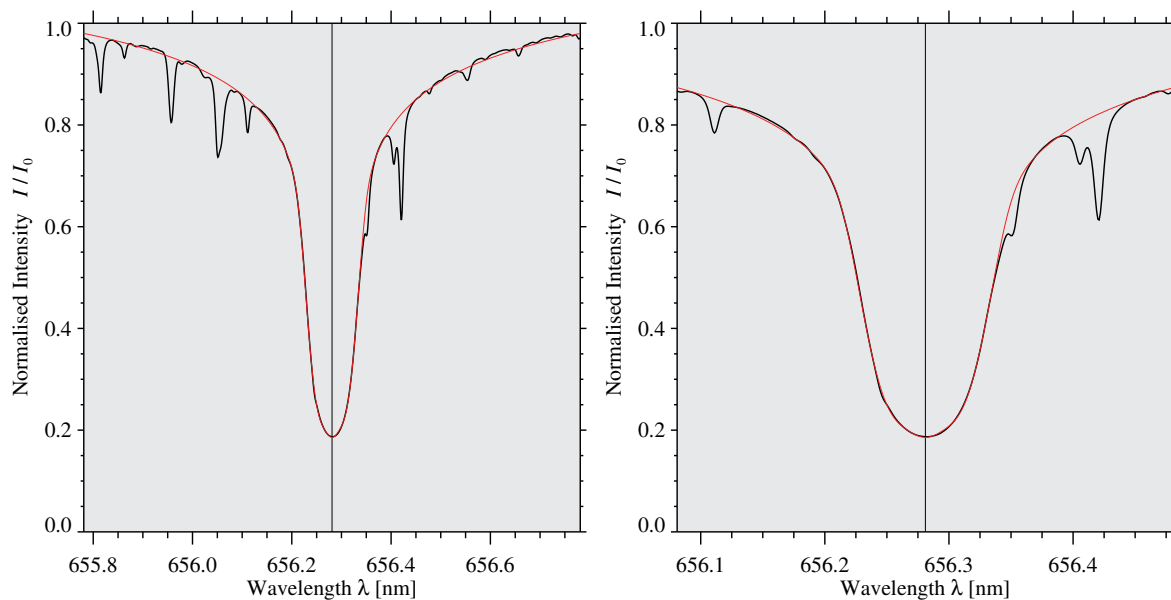


Figure 7.6: Disc-integrated H α quiet-Sun average profile (*black*) and the corresponding fit based on Voigt functions (*red*) for the entire spectral range (*left*) and for the immediate line core (*right*).

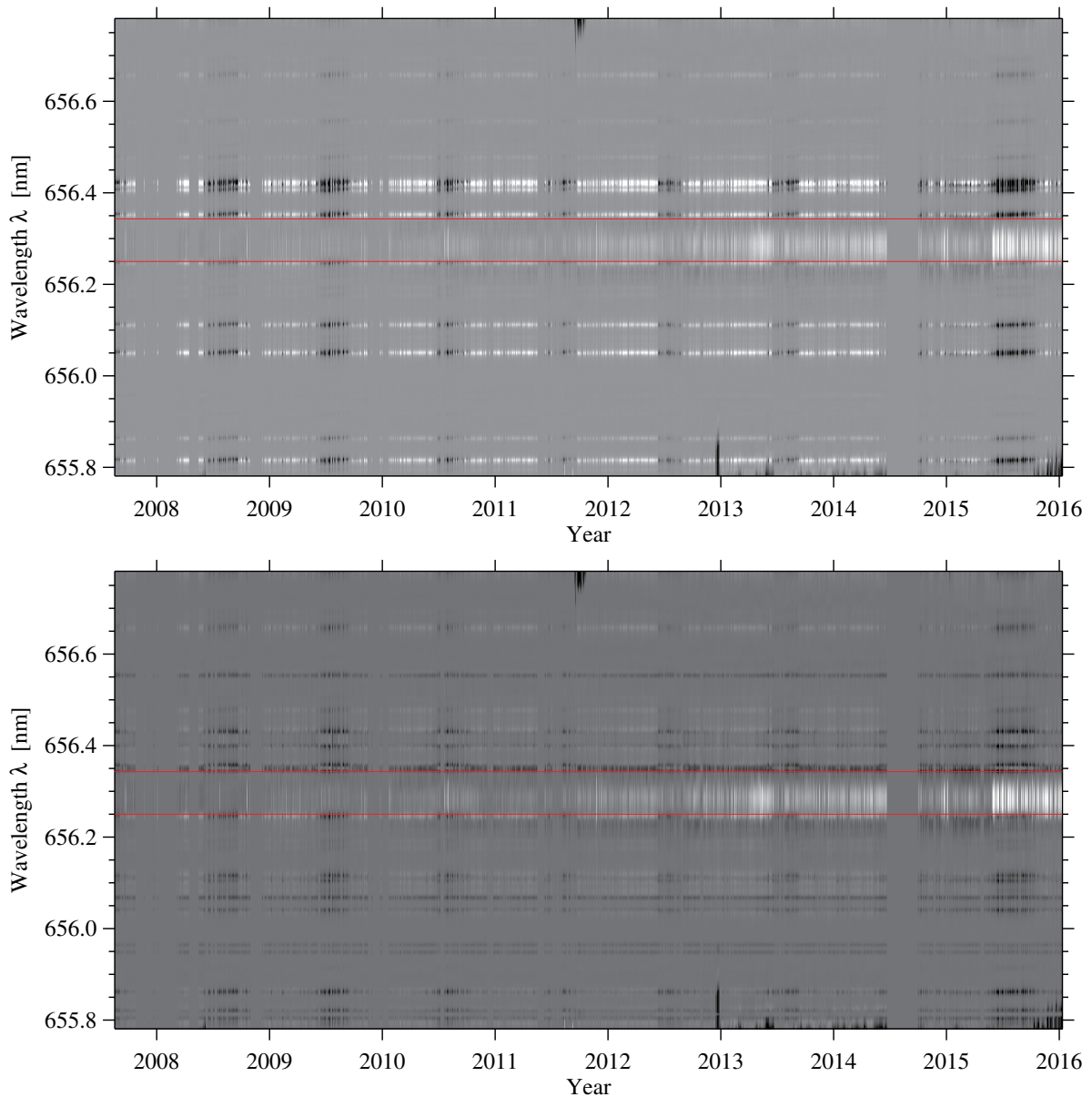


Figure 7.7: Collage of contrast profile scaled in the range of ± 0.1 for the *top* and in the range of -0.05 to 0.1 for the *bottom* plot, where the wavelength is given on the ordinate and the date on the abscissa. The two horizontal red lines indicate the spectral region with enhanced contrast in $H\alpha$. Other strong spectral signatures arise from telluric lines, which reflect changes in the Earth atmosphere (mostly the column density of water vapour) along the LOS. The data gap in late 2014 was caused by relocating SOLIS/ISS from KPNO to NSO headquarters in Tucson, Arizona.

area at an altitude of about 700 m. These changes are visible not just in the line core of $H\alpha$ but also in the strength of telluric lines, thus suggesting an instrumental effect.

Figure 7.8 illustrates the spectral region with enhanced contrast in $H\alpha$ around the line core marked by the two horizontal red lines visible in Fig. 7.7. More accurately, it shows the total contrast as a function of time, where, again, the data gap in late 2014 was caused by relocating SOLIS/ISS. Comparing this plot to the sunspot number or Mg II light curve, similarities are revealed, at least until mid 2014. Around May 2013 we can see a peak in the contrast plot but also in the sunspot timeseries of Fig. 6.1. For this time we were checking the contrast profiles for each spectrum and found that on 26 May 2013 the contrast was high and numerous filaments

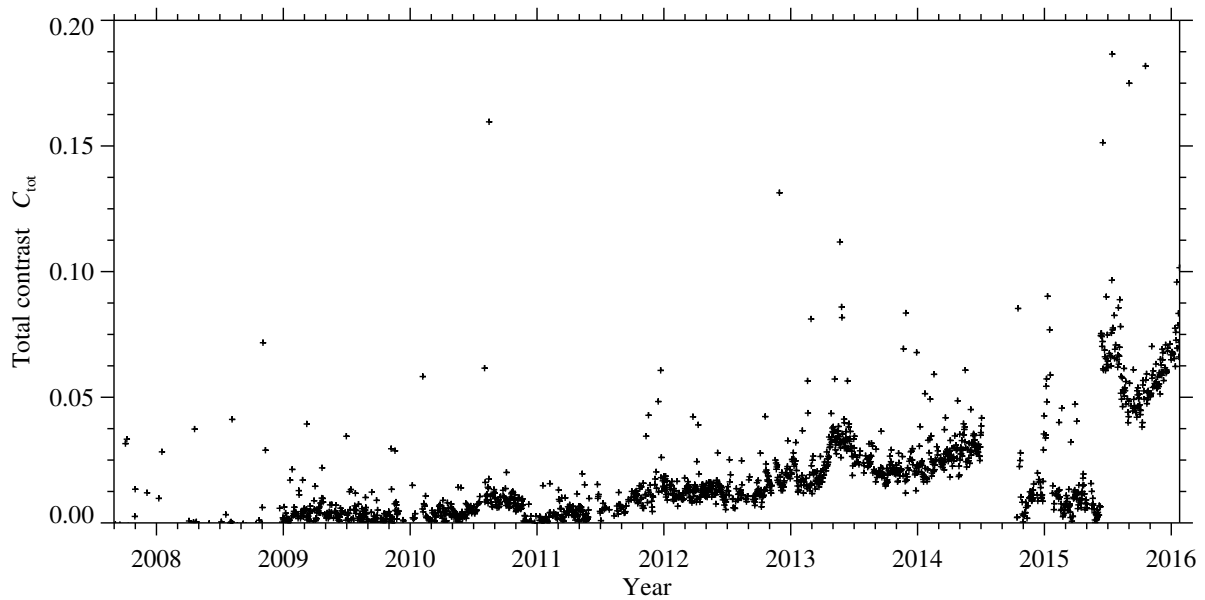


Figure 7.8: Total contrast as a function of time derived from the data in Fig. 7.7. The data gap in late 2014 was caused by relocating SOLIS/ISS from KPNO to NSO headquarters in Tucson, Arizona.

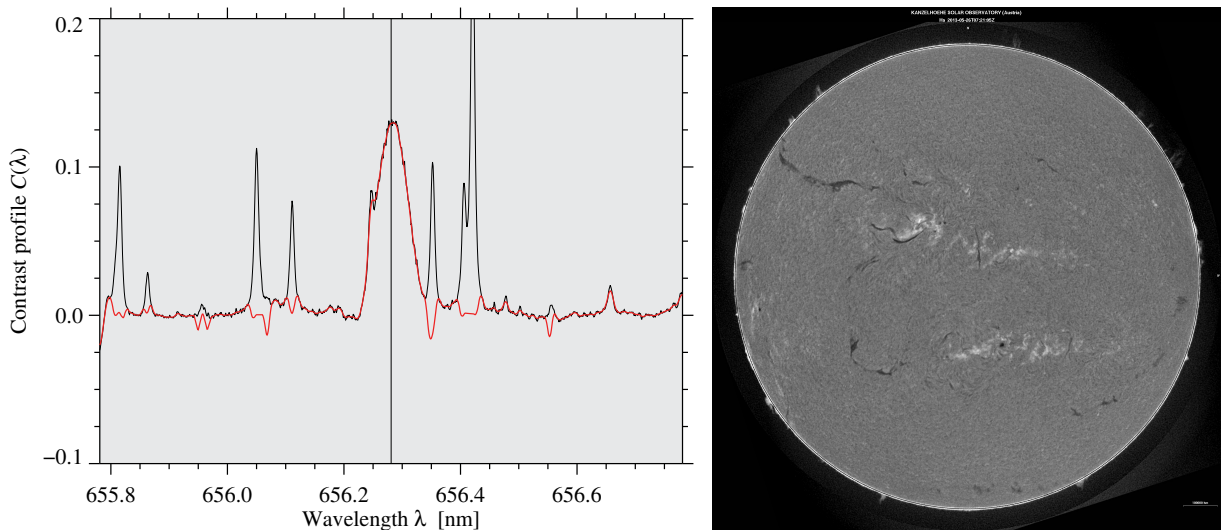


Figure 7.9: Observed (*black*) and fitted (*red*) contrast profiles for a day with high contrast in $H\alpha$ (*left*), where the vertical line marks the central wavelength. The corresponding full-disc image on 26 May 2013 (*right*), shows clearly that the Sun was active, as is evident in $H\alpha$ by extended dark filaments, mostly located in the northern hemisphere, and the bright plages in the two equatorial active region belts.⁶

were present on the solar surface, as depicted in Fig. 7.9. For the same day, we then tried an CM inversion of the contrast profile using a Levenberg-Marquardt⁵ fitting algorithm to obtain the CM parameters representing the entire solar disc.

In Fig. 7.9 (*left*) we fitted the contrast profile with a triple Voigt function using the Levenberg-Marquardt least-squares fitting algorithm. Now we want to fit the contrast profile of one specific day with the cloud model to obtain physical parameters of the Sun and thus explain our index physically (see Fig. 7.10). The parameters that we get by applying the cloud model are the

⁵<http://idlastro.gsfc.nasa.gov/ftp/pro/markwardt/mpfit.pro>

⁶http://cesar.kso.ac.at/synoptic/ha4m_days.php?year=2013[accessed 08 March 2016]

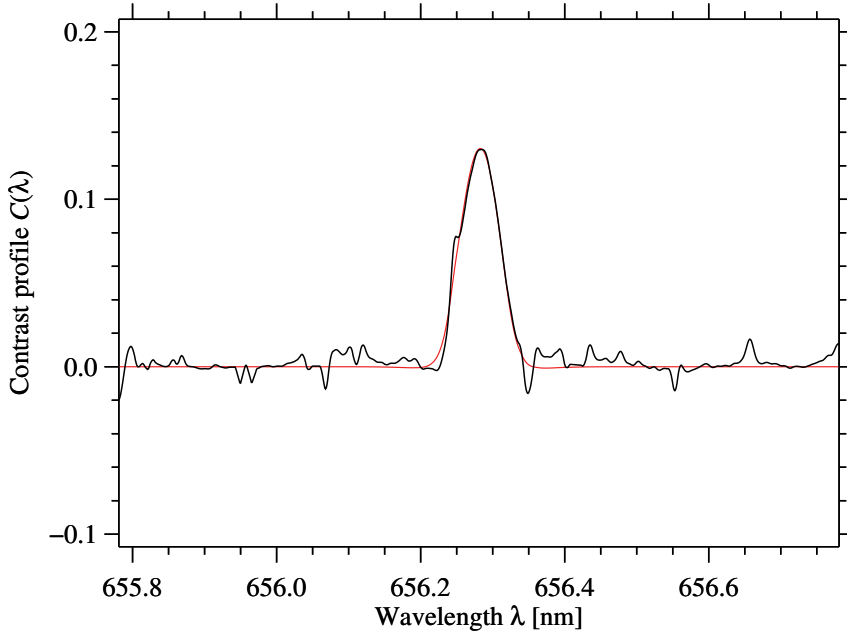


Figure 7.10: Fitting of the contrast profile with the CM using a Levenberg-Marquardt least-squares fit *red*. The fit around the line core with the CM just matches the contrast profile.

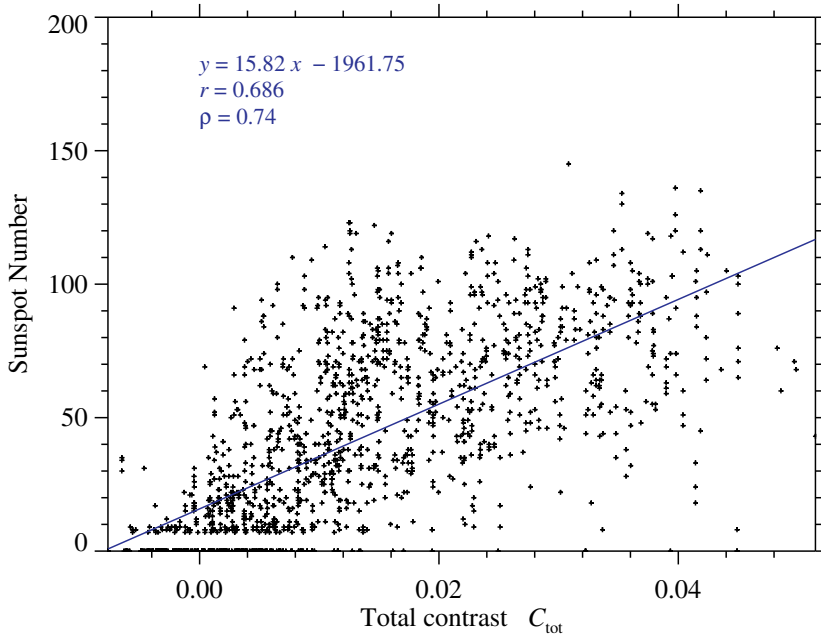


Figure 7.11: Scatter plot of the total contrast index and the SSN reveals a good correlation between the two indices.

optical thickness τ , the LOS Doppler velocity v_{LOS} , the Doppler width $\Delta\lambda_D$, and the source function S . Therefore, the programme used first needs estimated parameters in order to be able to start with some reasonable values. Furthermore, the programme needs a weighting scheme to know which of the fitted points should receive a higher weight when calculating the fit. Finally, we also need to set the limits for each parameter. We set the weighting to be equal for all points and the parameter limits to $\tau \in [0.01, 2]$, $v_{LOS} \in [-40, 40]$, $\Delta\lambda_D \in [20, 100]$, and $S \in [0.05, 1]$. With the non-linear Levenberg-Marquardt least-squares fit, we arrived at the four parameters $\tau = 0.05$, $v_{LOS} = 3.44$, $\Delta\lambda_D = 68.8$, $S = 0.63$. As the limits and, therefore, v_{LOS} and $\Delta\lambda_D$ are given in pixels, we have to convert these and obtain $v_{LOS} = 1575.45 \text{ m/s}$ and $\Delta\lambda_D = 688.18 \text{ m\AA}$.

The fit matches the contrast profiles well, but the most important results are, however, the parameters yielded by the fit. What is striking here is the high velocity and source function that

we obtain from the model. Considering that the fit parameters represent the entire solar disc implies that filaments might even exhibit higher velocities or that small-scale features possess a significant bulk velocity. The large source function might be linked to the presence of extended plage regions along the two equatorial belts.

This means that applying the CM to Sun-as-a-star $H\alpha$ data requires a much deeper investigation, which is beyond the scope of this Master thesis. However, as Fig. 7.11 reveals, the total contrast – sunspot number scatter plot shows a high correlation of our fitted total contrast activity index and the photospheric sunspot number activity index. For this plot, we took out 24 outliers that showed an extremely high total contrast. The gap, parallel to the abscissa is again due to the definition of the sunspot number. The scatter plot shows that we can find hints of chromospheric activity variation, not only in Ca II K, but also in $H\alpha$ with a correlation coefficient of $r = 0.686$ or $\rho = 0.74$.

Chapter 8

Conclusion

In the present work, our aim was to find a chromospheric Sun-as-a-star activity index in $H\alpha$ based on data of the Integrated Sunlight Spectrometer as part of the SOLIS telescope. The spectrometer takes spectra in $H\alpha$ on a daily basis to study changes in the solar irradiance along the solar cycle and the correspondence of the solar atmospheric layers to the solar magnetic activity. We analysed these spectra and the change of the absorption line with time, as this is related to physical parameters of the atmosphere. Additionally, we wanted to apply the cloud model to fit the spectral line in order to infer physical explanation for our index.

For that purpose, we first checked the data by reconstructing plots found in Bertello *et al.* (2011). The plots therein present activity parameters that can be inferred from the Ca II K line with improved data reduction for a better accuracy of the parameters. To construct the plots, a second-degree polynomial is plotted into the minima and maxima of the spectral line to find the best estimated minimum or maximum. We extended the period for which the time series of those parameters were plotted and found that it almost matches the plots of Bertello *et al.* (2011), which data for the plot is provided on the NSO website. However, there is a small offset and trend, which is caused by the code Bertello *et al.* (2011) used, which includes an additional normalisation (Bertello, priv. communication). Comparing our reconstructions to the new plots found on the NSO website since 6 November 2015,¹ we can however say that the plots now match and we have handled the data correctly.

To be able to classify our activity index with other indices, we present the SSN, F10.7cm Radio Flux, the MgII and the TSI indices in Chap. 6. The light curves of each index depicted therein show a clear correlation with the solar cycle. Scatter plots of two indices there indicate the correlation of an index and the related atmospheric layer with another index and its corresponding layer. We found that the indices correlate very well with each other, especially the SSN index and the F10.7 cm Radio Flux index have a high correlation, whereas the scatter plots involving TSI data do not have a good correlation with the other indices. This could be due to

¹http://solis.nso.edu/0/iss/iss_timeseries.html

the difficulty of calibrating TSI data and the fact that TSI does not change much over the solar cycle, but the SSI can change, for example in the UV, up to 100%.

As the solar spectra in $H\alpha$ reveal properties of the chromosphere, its time-series gives us an idea of the chromospheric variability during the course of a solar cycle. In addition, the chromospheric activity is related to magnetic field strength and the transition region and the corona. The $H\alpha$ data that we are using to develop our index is constructed the same as the Ca II K data used in Chap. 5. This means, the data are Sun-as-a-star data and are, therefore, spectra which are integrated over the entire solar disc. As opposed to the $H\alpha$ spectrum at the limb, the spectrum observed at disc-centre shows wider wings and a deeper line, hence we should be aware of the different shape of spectral lines in respect to the region they are observed at.

Applying the cloud model has so far only been done for a certain region on the solar disc and not for the integrated spectrum, as we used it in this work. To compute the contrast profile with the CM, we need a reference profile which in our case is the integrated quiet-Sun profile in $H\alpha$. We fitted both, the observed spectrum as well as the average quiet-Sun spectrum with a triple Voigt function using the Levenberg-Marquardt least-squares fitting algorithm. Having done that, we continued by investigating the intensity of the contrast profiles as a function of time. The total value of the contrast profiles yields the Sun-as-a-star chromospheric activity index.

To be able to draw conclusion about our index, we fitted our contrast profile with the CM and Levenberg-Marquardt least-squares fit to obtain the physical parameters of the structure that lies higher than the region in the atmosphere, where the lines evolve. The physical parameters that we obtain have to be interpreted with care because several assumptions of the cloud model might not be valid, e.g., 1D radiative transfer vs. a 3D geometry for full-disc observations. Especially, we cannot explain the high values of the velocity and source function that we get with the CM inversion technique.

What we could have done, if the time had allowed, is trying to find an even better first fit (with the Voigt function) of the contrast profile and remove all other telluric lines to yield a smooth curve. What else could be done following the present work is creating an algorithm to find the initial parameters, which have to be given to the programme, automatically. Now we have done it manually for one spectrum and it would be very tedious to do this for 2100 spectra. Based on many spectra, the conclusion about the physical parameters will be more sound.

The cloud model that we use is a reliable technique to obtain physical parameters of certain features on the solar disc, which has been used by many scientists before. However, it has only been used locally and not for disc-integrated spectra. As features on the solar disc and quiet-Sun regions cancel out when integrating over the solar disc, the contrast of our spectra with the quiet-Sun spectra is low and applying the cloud model is challenging. In addition,

the assumptions that are implied in the cloud model (e.g. that the background profile, here the averaged quiet-Sun profile, is the same as the incident light on the structure) can lead to a different result. For example, if the structure we want to investigate is embedded into the chromosphere and does not lie above the chromosphere, the incident light is different than the light coming from the chromosphere. An alternative solution of this problem is given by [Chae \(2014\)](#) with the Embedded Cloud Model (ECM) and for other improvements of the CM and its inversion technique to get physical parameters see [Tziotziou \(2007\)](#).

Finally, we produced a scatter plot of the $H\alpha$ index and the SSN data from Chap. 6. This showed how well the $H\alpha$ index, which represents the solar chromospheric activity, correlates with the SSN and therefore the photospheric activity of the Sun.

As each index represents the activity in a certain layer of the Sun, we could draw conclusions from the general to the small, meaning from the integrated spectra to atmospheric features. This could then be applied to other stars, and we can, only having their integrated spectrum, make suggestions about their atmospheric composition and structure.

Bibliography

- Balasubramaniam, K.S., Pevtsov, A.: 2011, Ground-Based Synoptic Instrumentation for Solar Observations. In: *Solar Physics and Space Weather Instrumentation IV, Proceedings of SPIE*.
- Beckers, J.M.: 1964, A Study of the Fine Structures in the Solar Chromosphere. PhD thesis, Sacramento Peak Observatory, Air Force Cambridge Research Laboratories, Mass., USA.
- Bertello, L., Ulrich, R., Boyden, J.: 2010, The Mount Wilson Ca II K Plage Index Time Series. *sp* **264**, 31 – 44. doi:[10.1007/s11207-010-9570-z](https://doi.org/10.1007/s11207-010-9570-z).
- Bertello, L., Pevtsov, A.A., Harvey, J.W., Toussaint, R.M.: 2011, Improvements in the Determination of ISS Ca II K Parameters. *Sol. Phys.* **272**, 229 – 242. doi:[10.1007/s11207-011-9820-8](https://doi.org/10.1007/s11207-011-9820-8).
- Bethge, C., Peter, H., Kentischer, T., Halbgewachs, C., Elmore, D., Beck, C.: 2011, The Chromospheric Telescope **534**. doi:[10.1051/0004-6361/201117456](https://doi.org/10.1051/0004-6361/201117456).
- Bostanci, Z.F., Al Erdoğan, N.: 2010, Cloud Modeling of a Quiet Solar Region in H α . *an* **81**, 769.
- Bouvier, J., Bertout, C., Benz, W., Mayor, M.: 1986, Rotation in T Tauri Stars. I - Observations and Immediate Analysis **165**, 110 – 119.
- Chae, J.: 2014, Spectral Inversion of the H α Line for a Plasma Feature in the Upper Chromosphere of the Quiet Sun. *Astrophys. J.* **780**, 109. doi:[10.1088/0004-637X/780/1/109](https://doi.org/10.1088/0004-637X/780/1/109).
- David, K.H.: 1961, Die Mitte-Rand-Variation der Balmerlinien H α – H δ auf der Sonnenscheibe. *Veroeffentlichungen der Universitaets-Sternwarte zu Goettingen* **7**, 367 – 399.
- De Pontieu, B., Erdélyi, R., James, S.P.: 2004, Solar Chromospheric Spicules from the Leakage of Photospheric Oscillations and Flows. **430**, 536 – 539. doi:[10.1038/nature02749](https://doi.org/10.1038/nature02749).
- Fröhlich, C.: 2011, Total Solar Irradiance: What Have We Learned from the Last Three Cycles and the Recent Minimum? *Space Sci. Rev.* **176**, 237 – 252. doi:[10.1007/s11214-011-9780-1](https://doi.org/10.1007/s11214-011-9780-1).
- Haigh, J.D., Lockwood, M., Giampapa, M.S.: 2004, *The sun, solar analogs and the climate*, Springer, Berlin Heidelberg.

- Haigh, J.: 2007, The Sun and the Earth's Climate. *Living Reviews in Solar Physics* **4**. doi:[10.12942/lrsp-2007-2](https://doi.org/10.12942/lrsp-2007-2).
- Hanisch, R.J., Farris, A., Greisen, E.W., Pence, W.D., Schlesinger, B.M., Teuben, P.J., Thompson, R.W., Warnock, A.: 2001, Definition of the Flexible Image Transport System (FITS). *Astron. Astrophys.* **376**, 359–380. doi:[10.1051/0004-6361:20010923](https://doi.org/10.1051/0004-6361:20010923).
- Hanslmeier, A.: 2002, *The sun and space weather*, Kluwer Academic Publishers, Dordrecht, Netherlands.
- Hathaway, D.H.: 2010, The solar cycle. *Living Reviews in Solar Physics* **7**(1). doi:[10.12942/lrsp-2010-1](https://doi.org/10.12942/lrsp-2010-1).
- Hoyt, D.V., Schatten, K.H.: 1997, *The role of the sun in climate change*, Oxford University Press, New York.
- Keil, S.L., Henry, T.W., Fleck, B.: 1998, NSO/AFRL/Sac Peak K-line Monitoring Program. In: Balasubramaniam, K.S., Harvey, J., Rabin, D. (eds.) *Synoptic Solar Physics, Astronomical Society of the Pacific Conference Series* **140**, 301.
- Keller, C.U.: 1998, SOLIS: A Modern Facility for Synoptic Solar Observations. In: Stepp, L.M. (ed.) *Advanced Technology Optical/IR Telescopes VI, Society of Photo-Optical Instrumentation Engineers (SPIE) Conference Series* **3352**, 732–741.
- Keller, C.U., Harvey, J.W., Giampapa, M.S.: 2003, SOLIS: An Innovative Suite of Synoptic Instruments. In: Keil, S.L., Avakyan, S.V. (eds.) *Innovative Telescopes and Instrumentation for Solar Astrophysics, Society of Photo-Optical Instrumentation Engineers (SPIE) Conference Series* **4853**, 194–204.
- Krivova, N.A., Solanki, S.K., Floyd, L.: 2006, Reconstruction of Solar UV Irradiance in Cycle 23. *Astron. Astrophys.* **452**, 631–639. doi:[10.1051/0004-6361:20064809](https://doi.org/10.1051/0004-6361:20064809).
- Krivova, N.A., Solanki, S.K., Schmutz, W.: 2011, Solar Total Irradiance in cycle 23. *Astron. Astrophys.* **529**, A81. doi:[10.1051/0004-6361/201016234](https://doi.org/10.1051/0004-6361/201016234).
- Kutner, M.L.: 2003, *Astronomy – a physical perspective*, Cambridge University Press, Cambridge.
- Lee, D.T., Schachter, B.J.: 1980, Two Algorithms for Constructing a Delaunay Triangulation. *Int. J. Comp. Inform. Sci* **9**, 219–242.
- Lilensten, J., Bornarel, J.: 2006, *Space weather, environment and societies*, Springer, Dordrecht, Netherlands.
- Mackay, D., Karpen, J., Ballester, J., Schmieder, B., Aulanier, G.: 2010, Physics of Solar Prominences: II Magnetic Structure and Dynamics. *Space Sci. Rev.* **151**, 333–399. doi:[10.1007/s11214-010-9628-0](https://doi.org/10.1007/s11214-010-9628-0).

- Mullan, D.: 2010, *Physics of the Sun*, CRC Press, Newark, USA.
- Pevtsov, A.A., Bertello, L., Marble, A.R.: 2014, The Sun-as-a-Star Solar Spectrum. *Astron. Nachr.* **335**, 21–26. doi:[10.1002/asna.201312012](https://doi.org/10.1002/asna.201312012).
- Pevtsov, A., Bertello, L., Uitenbroek, H.: 2013, On Possible Variations of Basal Ca II K Chromospheric Line Profiles with the Solar Cycle. *Astrophys. J.* **767**, 56–62. doi:[10.1088/0004-637X/767/1/56](https://doi.org/10.1088/0004-637X/767/1/56).
- Phillips, A.C.: 1994, *The Physics of Stars*, John Wiley and Sons Ltd, West Sussex.
- Press, W.H., Teukolsky, S.A., Vetterling, W.T., Flannery, B.P.: 2002, *Numerical recipes in c (2nd ed.): The art of scientific computing*, Cambridge University Press, New York, NY, USA.
- Skumanich, A., Lean, J., Livingston, W., White, O.: 1984, The Sun as a Star – Three-Component Analysis of Chromospheric Variability in the Calcium K Line. *Astrophys. J.* **282**, 776–783. doi:[10.1086/162262](https://doi.org/10.1086/162262).
- Solanki, S.K., Unruh, Y.C.: 2013, Solar Irradiance Variability. *Astron. Nachr.* **334**, 145–150. doi:[10.1002/asna.201211752](https://doi.org/10.1002/asna.201211752).
- Stix, M.: 2002, *The Sun*, Springer, Berlin.
- Strassmeier, K.G., Ilyin, I., Järvinen, A., Weber, M., Woche, M., Barnes, S.I., Bauer, S.M., Beckert, E., Bittner, W., Bredthauer, R., Carroll, T.A., Denker, C., Dionies, F., DiVarano, I., Döscher, D., Fechner, T., Feuerstein, D., Granzer, T., Hahn, T., Harnisch, G., Hofmann, A., Lesser, M., Paschke, J., Pankratow, S., Plank, V., Plüschke, D., Popow, E., Sablowski, D.: 2015, PEPSI: The High-Resolution Échelle Spectrograph and Polarimeter for the Large Binocular Telescope. *Astron. Nachr.* **336**, 324–361. doi:[10.1002/asna.201512172](https://doi.org/10.1002/asna.201512172).
- Thuillier, G., Deland, M., Shapiro, A., Schmutz, W., Bolsée, D., Melo, S.M.L.: 2012, The Solar Spectral Irradiance as a Function of the MgII Index for Atmosphere and Climate Modelling. *Sol. Phys.* **277**, 245–266. doi:[10.1007/s11207-011-9912-5](https://doi.org/10.1007/s11207-011-9912-5).
- Tziotziou, K.: 2007, Chromospheric Cloud-Model Inversion Techniques. In: Heinzl, P., Dorotovič, I., Rutten, R.J. (eds.) *The Physics of Chromospheric Plasmas*, *Astronomical Society of the Pacific Conference Series* **368**, 217–237.
- Usoskin, I.G.: 2013, A History of Solar Activity over Millennia. *Living Reviews in Solar Physics* **10**. doi:[10.12942/lrsp-2013-1](https://doi.org/10.12942/lrsp-2013-1).
- Viereck, R., Puga, L.: 1999, The NOAA MgII Core-to-Wing Solar Index: Construction of a 20-Year Time series of Chromospheric Variability from Multiple Satellites. *J. Geophys. Res.* **104**, 9995–10006. doi:[10.1029/1998JA900163](https://doi.org/10.1029/1998JA900163).

- Ward-Thompson, D., Whitworth, A.P.: 2011, *An Introduction to Star Formation*, Cambridge University Press, Cambridge.
- Weigert, A., Wendker, H., Wisotzki, L.: 2011, *Astronomie und Astrophysik*, Wiley-VCH, Weinheim.
- Wells, D.C., Greisen, E.W., Harten, R.H.: 1981, FITS – A Flexible Image Transport System. *Astron. Astrophys. Suppl. Ser.* **44**, 363 – 370.
- Wilson, O.C.: 1978, Chromospheric Variations in Main-Sequence Stars. *Astrophys. J.* **226**, 379 – 396. doi:[10.1086/156618](https://doi.org/10.1086/156618).
- Zeilik, M., Gregory, S.: 1998, *Introductory Astronomy & Astrophysics*, Thomson Learning, USA.
- Zirker, J.B.: 2001, *Journey from the Center of the Sun*, Princeton University Press, Princeton.

Acknowledgments

First of all, I would like to thank my supervisor Prof Dr Carsten Denker. Thank you for literally being *super* kind, which makes working with you and your group a great pleasure! You have always been patient and happy to help, even if you are very busy yourself. You do take care of your group and your students and make sure they are fine. Thank you for your explanations regarding all my questions about physics, for proof-reading, your support, and encouragement throughout the thesis as well. You are a great person and I could not have asked for a better supervisor!

I would like my to thank my co-advisor Prof Dr Gottfried Mann for being very kind and for offering help at any time as well.

Thanks to my office colleagues, Andrea Diercke, Dr Christoph Kuckein and Sergio Gonzalez, for a fun time in the office, and also the rest of the Optical Solar Physics group of the AIP, especially Dr Meetu Verma and Dr Horst Balthasar for your help and support as well.

I also want to thank Dr Yvonne Unruh for introducing me into the world of science during my internship, an awesome time at Imperial College, and proof-reading the first drafts. Moreover, I would like to thank Andrea Diercke, Horst Balthasar and Marcel Weiss for proof-reading pieces of my work, too. And a big thank you also goes to Dr Jonathan Tottle for your brilliant explanations at any given time, as well as proof-reading the whole thesis! Thank you very much, Jochen Heinz, for your friendship, support, as well as a place to crash at after looong office hours and caring for me when I was ill or hungry (:D) during the course (especially at the end) of writing up this thesis.

In addition, I would like to thank my friend Katie for proof-reading in her amazing English (:D). And I want to thank all my other friends as well, especially Cindy, Jennifer, Margit and Susann, for supporting, encouraging and believing in me.

Furthermore, I would like to express my special thank to my sisters Milly and Thao who supported me with their technical knowledge, mental strength and wise words throughout the thesis, and my parents for their endless love. Thank you, to my partner Mathias for your love, your understanding for whenever I had to do some work and for your support, as well. I appreciate and love you all very much.

Last but not least, this work would not have been possible without the people behind the data calibration. Thanks to the National Solar Observatory for providing easily accessible SOLIS / ISS data, which constitute the main data set I have used for this thesis. A special thanks goes to Dr Luca Bertello for his readiness to help and his very quick and kind responses. Moreover, I would like to thank the Sunspot Index and Long-term Solar Observations (SILSO) for providing the sunspotnumber data, the Space Physics data Facility of the Goddard Space Flight Center for

the F10.7cm Radio Flux data, the University of Bremen for the MgII composite data and the University of Colorado Solar Radiation and Climate Experiments (SORCE) for the TSI data.

Appendix A – List of Acronyms

AIP	Leibniz-Institut für Astrophysik Potsdam
CM	(Beckers) Cloud Model
CCD	Charge-Coupled Device
CM	Cloud Model
CME	Coronal Mass Ejection
FITS	Flexible Image Transport System
HRD	Hertzprung-Russel-Diagram
IDL	Interactive Data Language
ISN	International Sunspot Number
ISS	Integraed Sunlight Spectrometer
KPNO	Kitt Peak National Obervatory
LOS	Line-Of-Sight
Mm	megametres
NSF	National Science Foundation
NSO	National Solar Observatory
PEPSI	Potsdam Echelle Polarimetric and Spectroscopic Instrument
SDI	Solar-Disk-Integrated (telescope)
SDO	Solar Dynamics Observatory
SOLIS	Synoptic Optical Long-term Investigations of the Sun
SSI	Spectral Solar Irradiance
TSI	Total Solar Irradiance
UV	UltraViolet

Selbstständigkeitserklärung

Hiermit erkläre ich, dass ich diese Arbeit selbständig verfasst und keine anderen als die von mir angegebenen Hilfsmittel und Quellen genutzt habe.

Potsdam, 14. Mai 2016

Linh Le Phuong